Silvia Humer, BSc

From Superconductivity to Thermoelectricity: Ge based Skutterudites

MASTER THESIS

For obtaining the academic degree
Diplom-Ingenieurin

Master Programme of
Technical Physics

Graz University of Technology

Supervisor:

Univ.-Prof. Dipl.-Ing. Dr.techn. Ernst Bauer

Institut für Festkörperphysik, TU Wien

Graz, Juni 2011

Deutsche Fassung:
Beschluss der Curricula-Kommission für Bachelor-, Master- und Diplomstudien vom 10.11.2008
Genehmigung des Senates am 1.12.2008

EIDESSTATTLICHE ERKLÄRUNG

Ich erkläre an Eides statt, dass ich die vorliegende Arbeit selbstständig verfasst, andere als die angegebenen Quellen/Hilfsmittel nicht benutzt, und die den benutzten Quellen wörtlich und inhaltlich entnommene Stellen als solche kenntlich gemacht habe.

Graz, am 30.6.11 ..... Silvia Huber .....
(Unterschrift)

Englische Fassung:

STATUTORY DECLARATION

I declare that I have authored this thesis independently, that I have not used other than the declared sources / resources, and that I have explicitly marked all material which has been quoted either literally or by content from the used sources.

30.6.11 ..... Silvia Huber .....
date (signature)

Abstract

Two superconducting germanium based Skutterudite compounds ($\mathrm{LaPt_4Ge_{12}}$ and $\mathrm{BaPt_4Ge_{12}}$) were tried to be modified to get good thermoelectric properties, by substitution. A sample series of $\mathrm{LaPt_4Ge_{12-x}Sb_x}$ with $\mathrm{x} < 5$ could be produced by arc melting and annealing at 800°C for 10 days. The sample composition and quality was analyzed by X-ray powder diffraction at room temperature and in the electron microscope with micro probe analysis. The critical temperature $\mathrm{T_c}$ for superconductivity decreases very rapidly with increasing the Sb content $\mathrm{x} = 0, \mathrm{T_c} = 8.27$ K; $\mathrm{x} = 0.5, \mathrm{T_c} = 5.20$ K. They are type II BCS superconductors, which was verified by susceptibility and specific heat measurement. Seebeck effect increases from 3 $\mu\mathrm{V/K}$ for $\mathrm{x} = 0$ to 43 $\mu\mathrm{V/K}$ for $\mathrm{x} = 5$ at room temperature, resistivity at room temperature also increases with increasing antimony amount. The main reason for the the rapid increasing of the Seebeck coefficient is the charge carrier density, which was determined by Hall measurement. Furthermore phonon properties were investigated by thermal expansion and heat capacity measurement.

Kurzfassung

An zwei supraleitenden Germanium basierten Skutterudit Verbindungen ($\mathrm{LaPt_4Ge_{12}}$ und $\mathrm{BaPt_4Ge_{12}}$) wurde versucht, diese durch gezielte Substitution so zu verändern, dass sie gute thermoelektrische Eigenschaften aufweisen. Eine Probenreihe von $\mathrm{LaPt_4Ge_{12-x}Sb_x}$ mit $\mathrm{x} < 5$ konnte durch Schmelzen im Lichtbogenofen und Glühen bei 800°C für 10 Tage hergestellt werden. Die Zusammensetzung und Qualität der Proben wurde mittels Röntgen- Pulverdiffraktometrie und im Elektronenmikroskop mittels micro probe analysis festgestellt. Die kritische Temperatur T_c der Supraleitung sinkt sehr schnell mit einer Erhöhung des Sb-Gehalts: $\mathrm{x} = 0, \mathrm{T_c} = 8.27$ K, $\mathrm{x} = 0.5, \mathrm{T_c} = 5.20$ K. Die supraleitenden Proben sind Typ-II, BCS Supraleiter, was mittles Messung der Suszeptibilität und der spezifischen Wärme verifiziert wurde. Der Seebeck- Koeffizient steigt bei Raumtemperatur von 3 $\mu\mathrm{V/K}$ für $\mathrm{x} = 0$ auf 43 $\mu\mathrm{V/K}$ für $\mathrm{x} = 5$. Der Widerstand bei Raumtemperatur steigt ebenso mit zunehmender Menge an substituiertem Antimon. Der Grund für die rasche Erhöhung des Seebeck-Koeffizienten ist die verringerte Ladungsträgerdichte, welche mittels Hall-Messung ermittelt wurde. Außerdem wurden Gittereigenschaften durch Messung der thermischen Ausdehnung und der Wärmekapazität untersucht.

I want to thank my parents and my three sisters Christina, Barbara and especially Monika, who helped me in so many different ways.

Many thanks also to Stefan Laumann, Oscar Duran, Esmaeil Royanian and Matthias Ikeda, for showing me how to use the different physical instruments. I also want to thank all the other colleges from the TU Vienna for all the interesting discussions and inputs to my work, especially my office mates Luisa Hoppichler and Friedrich Kneidinger.

Furthermore I owe my thanks to Prof. Gerfried Hilscher, Prof. Herwig Michor and Prof. Herbert Müller for doing measurements for me.

I am also grateful to Prof. Peter Franz Rogl and his working group for helping me producing my samples, for giving me a desk and treating me like one of them.

I want to thank Prof. Ernst Bauer for giving me the opportunity to do research at his group and for providing such a pleasant and free work environment.

Table of Contents

1. Introduction

[1] Thermoelectricity as well as thermal conductivity and electrical conductivity is a bulk property driven by a temperature gradient or an electric field. However its the most fascinating one. If a temperature gradient is applied to a conductor without an electric field not only a heat flow occurs, but also electric current, due to thermodiffusion. Because of the charge of the electrons a field in the opposite direction is created. In order to measure this current the circuit has to be closed. Fig. 1.1 left, illustrates such a closed

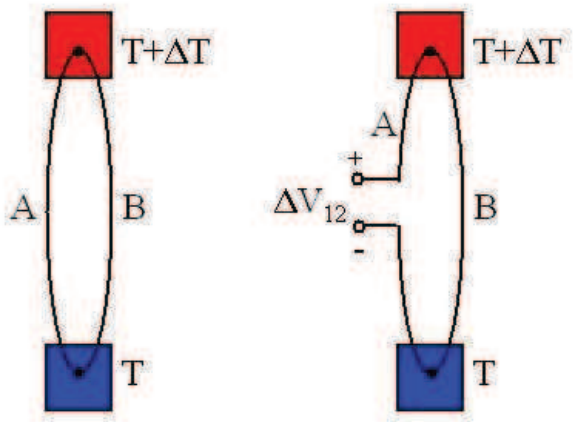

Figure 1.1.: Left: closed circuit; if material 1 and 2 are different thermoelectric current flows. Right: open circuit; if material 1 and 2 are different potential difference is generated

circuit. If material 1 and material 2 are the same, the same current flows in the left and the right arm of the circuit and so it cancels out and can not be measured, although it still is there. In order to measure this effect two different materials have to be used. The right side of Fig. 1.1 shows an open circuit; the observed thermoelectric potential is proportional to temperature difference and to the difference in thermoelectric properties of the bulk materials. It does not depend on size or dimension of the conductors, assuming that the dimensions are large compared to the mean free path of the electrons.

[1] From references: [1], [2], [3] and [4]

This thermoelectric potential was first observed in metals where Seebeck coefficients were around $10\mu\mathrm{V/K}$. Later, semiconductors were started to be investigated with much higher Seebeck coefficients, around $100\mu\mathrm{V/K}$ but also with higher resistivities. The best thermoelectric materials are somewhere in between; see section 2.2. Thermoelectric de-

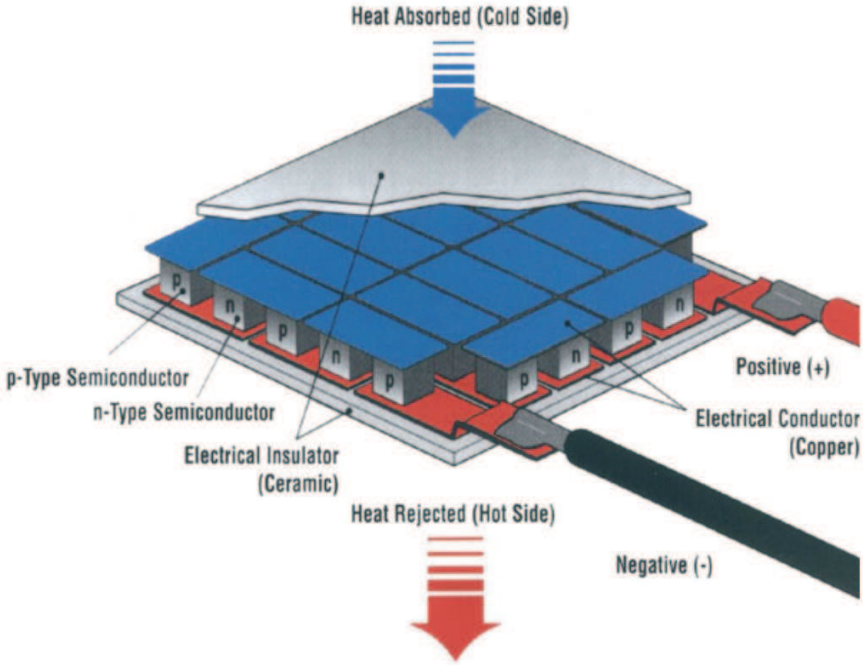

Figure 1.2.: thermoelectric device; taken from [4]

vices are made of a p- and a n-type legs connected with a metal; connected in series with the next couple, see Fig. 1.2. This increases the provided voltage. Using this devices to produce electrical energy out of thermal energy (for example waste heat) is the reason for intense research in this area. Such devices are small and work without moving parts and would therefore be very stable. Still the efficiency is quite low, so until now they are mainly used for niche applications, like power supply in space and conventional, mechanical heat engines are still much more efficient. According to Vining [2] the most promising applications for thermoelectric generator systems are small scaled (size and power scale) waste energy converters.

2. Theoretical aspects

2.1. Superconductivity

[1] Superconductivity is a quantum mechanical phenomenon; it is the vanishing of the electrical resistance in certain materials below a characteristic temperature $\mathrm{T_C}$, a characteristic field $\mathrm{H_C}$ and a characteristic current $\mathrm{J_C}$. At lower temperatures the superconducting state resists higher magnetic fields or currents. For conventional Type I superconductors, the most simple case, the relation between $\mathrm{T_C}$ and $\mathrm{H_C}$ is given in Eqn. 2.1 and shown in Fig. 2.1.

$$H_C(T) = H_C^0 \left[1 - \left(\frac{T}{T_C}\right)^2\right] \tag{2.1}$$

The critical current, that can also destroy the superconducting state, is approximately

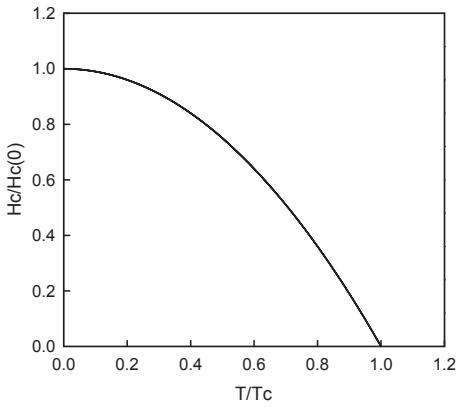

Figure 2.1.: Temperature dependence of the critical field

reached when the induced magnetic field at the surface of the sample equals the critical field. The superconducting state is also defined by the Meissner- Ochsenfeld effect. For small fields a superconductor can expel all applied magnetic fields by surface currents. It

[1] From reference [5]

is then a perfect diamagnetic material, with $\mathrm{B} \equiv 0$ within it.

$$B = \mu_0(H + M) = 0 \qquad \chi = \frac{dM}{dH} = -1 \tag{2.2}$$

While cooling down a sample in a field (FC) under $\mathrm{T_C}$ shielding currents arise in the superconductor surface. These currents create a field, such that inside the superconductor the applied and the induced field exactly cancel, while outside they add. This makes superconductivity being a thermodynamic state.

2.1.1. BCS theory

[2] The BCS theory is a microscopic theory of superconductivity, introduced 1957 by John Bardeen, Leon N. Cooper and John R. Schrieffer. The theory includes the formation of Cooper pairs out of electrons, caused by the presence of an attractive potential, coming from the lattice vibrations (electron-phonon-interaction). The wave function for these paired electrons is adjusted to minimize the free energy and gives the basis of the BCS theory. The gain of energy by the formation of Cooper pairs, out of electrons near the Fermi level, gives rise to an energy gap around the Fermi level. The gap size is proportional to ω_D, the Debye frequency because of this electron-phonon-interaction. Furthermore there is an exponential dependence on U, the electron-phonon-interaction potential and $\mathrm{N(E_F)}$, the density of states at the Fermi level.

$$\Delta = 2\hbar\omega_D \exp \frac{-1}{N(E_F)U} \tag{2.3}$$

The electronic part of the thermal conductivity is small as there are no states at $\mathrm{E_F}$ (because of the gap). The critical field, the transition temperature and the critical current are quantified by the energy gap and therefore strongly influenced by the density of states at the Fermi level. The connection to the transition temperature is Eqn. 2.4.

$$k_B T_C \approx 1.13\hbar\omega_D \exp \frac{-1}{N(E_F)U} \tag{2.4}$$

A magnetic field as well as a current (connected over Biot Savart law) cause an energy effort to exclude this field. This energy is proportional to B^2 so the critical field is where this excluding energy is equal to the gap energy. The temperature dependence of the

[2] From reference [6]

gap around $\mathrm{T_C}$ is in generally Landaus theory of second order phase transition.

$$\Delta(T)/\Delta_0 \cong 1.74\sqrt{1 - T/T_C} \tag{2.5}$$

$$\frac{C_S}{\gamma T_C} = 8.5 \exp -\frac{0.82\Delta_0}{k_B T} \tag{2.6}$$

The energy gap is often experimentally measured employing the specific heat Eqn. 2.6. γ stands for the Sommerfeld coefficient. $\mathrm{C_{eS}}$ is the specific heat of the superconducting state and in a real measurement it is gained by measuring also the specific heat of the normal state $\mathrm{C_n}$ (using a magnetic field $\mathrm{H} > \mathrm{H_C}$) and subtracting it. The specific heat jumps at a fixed value at $\mathrm{T} = \mathrm{T_C}$ and falls off exponentially.

$$\frac{\Delta C}{C_n}(T = T_C) \equiv \frac{C_{eS} - C_n}{C_n}|_{T=C_C} = 1.43 \tag{2.7}$$

2.1.2. Type I / type II superconductors

[3] Type I superconductors switch, while increasing the magnetic field, abruptly from Meissner state to normal state. This means switching from no penetration of magnetic field to full penetration at the critical field H_C. Increasing the magnetic field to $\mathrm{H_{c1}}$, type II superconductors switch from Meissner state to a mixed state. There, vortices carry flux lines with an elementary amount of flux $\phi_0 = \frac{h}{2e}$. Increasing until the second critical magnetic field $\mathrm{H_{c2}}$ the flux increases continuously until full flux penetration is reached in the normal state. The Ginzburg-Landau theory was originally introduced as a phenomenological theory of phase transitions. For temperatures close $\mathrm{T_C}$ the Ginzburg-Landau equations can be obtained from the BCS theory. Type I and type II superconductors are explained as a result of considerations concerning the temperature dependence of two characteristic length: the coherence lengths ξ and the penetration depth λ. The density of Cooper pairs $n_S = |\psi(\vec{r})|^2$ changes with this characteristic coherence length ξ. The penetration depth λ of the magnetic field can be gained from the London equations. Fig. 2.3 shows the meaning of λ and ξ and how they change starting from the surface. The interface energy between the superconducting phase and the normal conducting phase can be positive or negative. A negative interface energy means that the interface is as big as possible and that causes a division in small superconducting (without flux) and normal conducting (with flux) areas. This can be done until the quantum limit and is then a stable type II superconducting mixed state. The connection to the two parameters λ and

[3] From references [7], [8], [9], [10] and [11]

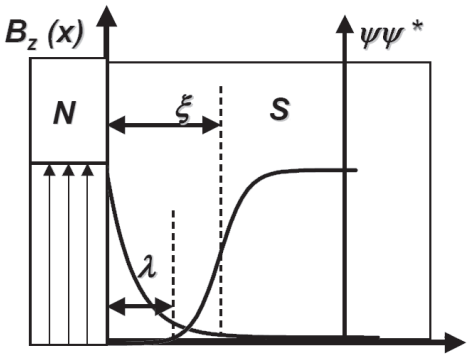

Figure 2.2.: interface energy in connection with λ and ξ; picture taken from [9]

ξ can be explained over the two energies connected with this parameters: the energy $\mathrm{E_B}$, that is necessary to eject the the magnetic field and the energy $\mathrm{E_c}$ gained by the condensation of the Cooper pairs. If $\lambda >> \xi$ the interface energy is positive, energy is needed to build this interfaces - type I superconductors. If $\lambda << \xi$, the energy needed to eject the the magnetic field at this surface $\mathrm{E'_B}$ is smaller than the energy gained by the condensation at this surface $\mathrm{E'_c}$ so the difference of this energy is the surface energy, that favors having big surfaces. This is realized as cylinder vortices with magnetic flux lines and normal conduction state inside and superconducting state outside .

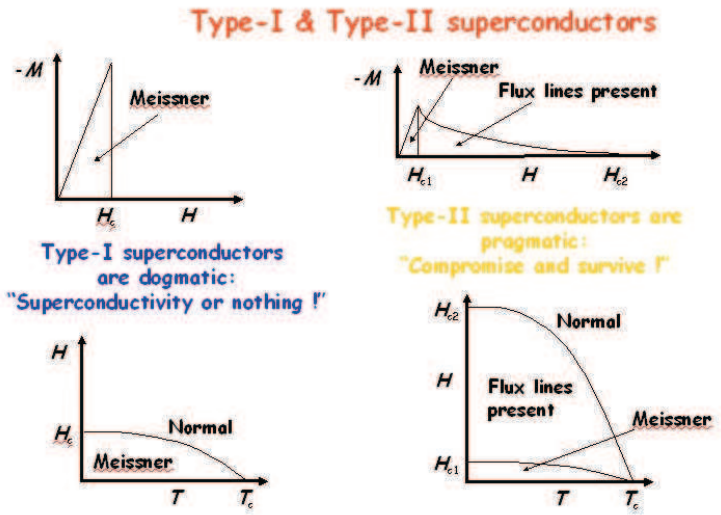

Figure 2.3.: Magnetization properties of Type I and Type II superconductors; picture taken from [10]

2.2. Optimization and selection of thermoelectric materials

[4] The transport parameters that influence the thermoelectric performance are carrier concentration, carrier mobility and effective mass, and lattice thermal conductivity. Optimization of this parameters is complex and a lot of times excludes each other.
The figure of merit ZT is used to compare the efficiency of Thermoelectric devices. It is defined as :

$$ZT = \frac{S^2 \sigma T}{\lambda} \tag{2.8}$$

where S is the Seebeck coefficient, λ is the thermal conductivity, σ the electrical conductivity and T the temperature.

2.2.1. Free charge carrier concentration

All the factors of Eqn. 2.8 are strongly influenced by the number of free charge carriers. The electrical conductivity depends on the the carrier concentration n and the mobility μ:

$$\sigma = ne\mu \tag{2.9}$$

For the electronic part of the thermal conductivity (in metals the dominating part) the WiedemannFranz law is valid:

$$\frac{\lambda_{el}}{\sigma} = LT = constT \tag{2.10}$$

with L the Lorenz number. So for metals the optimization of thermoelectric performance is limited to the optimization of the Seebeck coefficient, which is also strongly influenced by the charge carrier concentration. The Seebeck coefficient, for a single parabolic band with high charge carrier concentrations at high temperatures, can be written as:

$$S = \frac{8\pi^2 k_B^2}{3eh^2} m^* T \left(\frac{\pi}{3n}\right)^{2/3} \tag{2.11}$$

Figure 2.4 taken from [14] shows the optimum of the charge carrier concentration for $\mathrm{Bi_2Te_3}$. It is at about $10^{19} - 10^{21} \mathrm{carriers/cm^3}$ which is in the range of an heavily doped semiconductor.

[4] From references [12], [13] and [14]

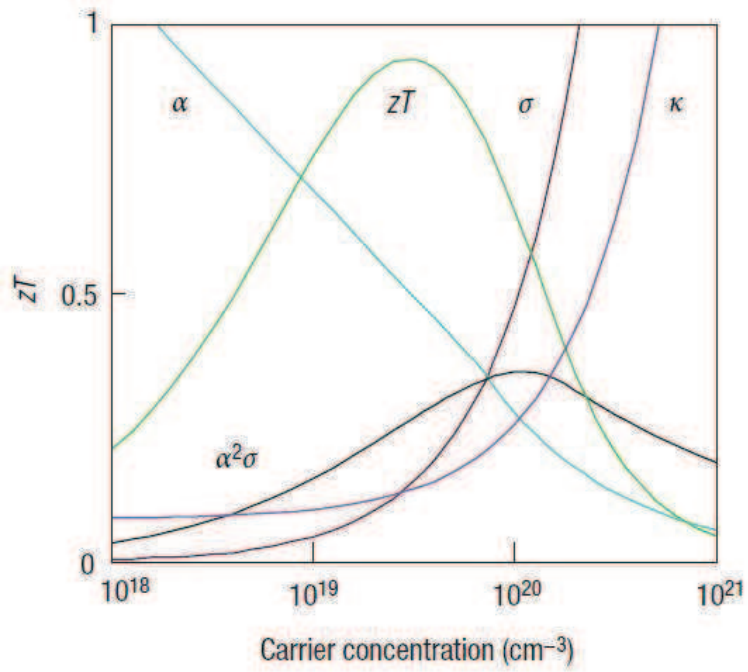

Figure 2.4.: Optimum of ZT with respect to charge carrier concentration. It is a compromise between the influence on of the free charge carrier concentration on the thermal conductivity κ, the Seebeck coefficient α and the electrical conductivity σ. A typical range for good thermo electrical materials is $10^{19} - 10^{21}$carriers/cm^3. Taken from reference: [14]

2.2.2. Mobility and effective mass

[5] Seebeck coefficient depends not only on the charge carrier density, but also on the effective mass, Eqn. 2.11. To get a big voltage between the hot and the cold end it is important to have only one type of charge carrier (electrons and holes move from the hot to the cold end). This is fulfilled by Fermi levels near the edge of a band gap. The sharper and higher the edge the better the Seebeck coefficient. A sharp and high edge at the density of states for single parabolic band model is equivalent to an high effective mass m*. High mobility increases the ZT by increasing the electric conductivity, Eqn.2.9. Mobility and effective mass are generally conflicting parameters, heavy charge carriers cause a low mobility. But mobility is also influenced by scattering processes, like electron phonon scattering, scattering with impurities, defects and grain boundaries.

2.2.3. Lattice thermal conductivity

[6] Considering Eqn. 2.8 and Eqn. 2.10 as well as the right side of Fig. 2.4 it can be seen that the electronic part of the thermal conductivity and of the electrical resistivity give a constant contribution ($\tilde{L}$) to the value of ZT. For metals ZT is mainly determined by the Seebeck coefficient. The lattice part of the thermal conductivity is tried to be minimized independently. So the material should be glass like for phonons and crystal like for electrons. One approach to reduce thermal lattice conductivity is to form nanostructured materials to increase phonon scattering on surfaces. Another is point defect scattering, by inducing vacancies or site substitutions. Clathrates and skutterudites form a cage that can be filled or partly filled with weakly bound big atoms, so called "rattlers". These "rattlers" are have been thought to move independently from the cage and act as some center of scattering. More likely the rattling effect is part of an more general cause of low lattice thermal conductivity λ_l: a large unit cell. The number of phonon modes is 3N, with N the number of atoms per unit cell. Every material has 3 acoustic modes and 3N-3 optical modes if there is more than one atom in each unit cell (N>1). The heat transport is performed primarily by the acoustic modes, because the group velocity of the high frequent optical modes is very low or even zero. The optical modes give a contribution to the internal energy and therefore to the heat capacity but not in a direct manner to the thermal conductivity.

[5] From reference [12]
[6] From reference [14]

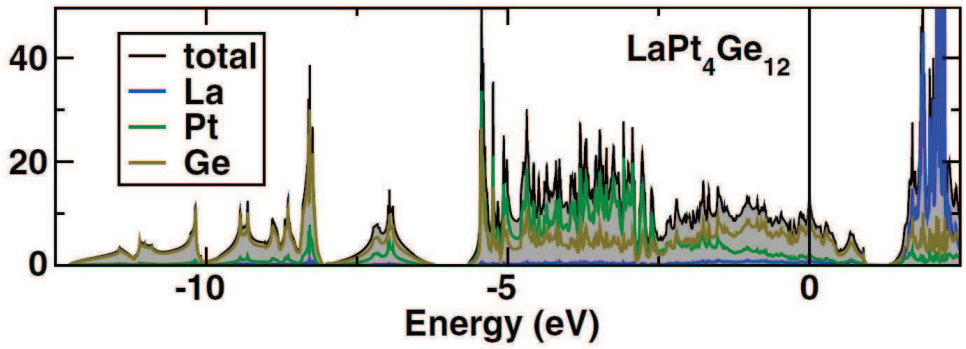

Figure 2.5.: density of states calculation of the Reference material $LaPt_4Ge_{12}$ taken from [17]. p Ge states are the dominating contribution at the Fermi level

2.2.4. Ge based skutterudites

[7] The two superconducting, metallic compounds: $BaPt_4Ge_{12}$ and $LaPt_4Ge_{12}$ consist on a framework of Ge and Pt, electronically stabilized by La/Ba cations. Looking at Fig. 2.5 for $LaPt_4Ge_{12}$ it can be observed that further electrons are needed to shift the Fermi energy towards the gap in the electronic density of states (DOS). For $BaPt_4Ge_{12}$ Fig. 2.6 shows the density of states (taken from [15]). Zintl phases consist of anions and cations, that donate their electrons to the electronegative anions. The bonding model is a mixture of ionic and covalent contributions. Classical Zintl phases (also called polar intermetallics) are valence balanced and semiconductors. An example for this is the prototype of the skutterudites $CoAs_3$. Zintl chemistry can be used to predict the electrical properties of the compounds through valence electron count. An increasing valence imbalance leads from semi conducting to metallic behavior; for more details see also reference [12]. Comparing $LaPt_4Ge_{12}$ with semi conducting $CoAs_3$ the structure has 12 electrons less from using As instead of Ge, 4 electrons more from using Pt instead of Co and three extra electrons from the filler Atom La. This very simple consideration predicts that $LaPt_4Ge_{12}$ shows p-type metallic behavior and that adding to this structure in some way 5 electrons leads to a semiconductor. For $LaPt_4Ge_{12}$ this was done by substituting Ge by Sb $LaPt_4Ge_{12-x}Sb_x$ x = 0,1,2,3,4,5,6,7. It can be seen later that this predictions is in quite good agreement with the experimental results.

[7] From reference [15], [12], [16] and [17]

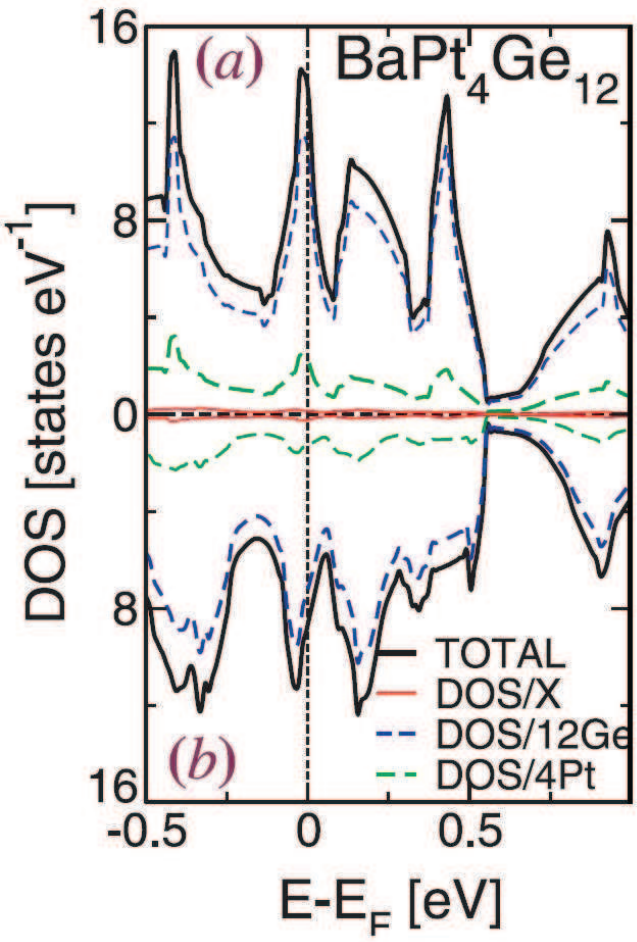

Figure 2.6.: density of states calculation of the Reference material $\mathrm{BaPt_4Ge_{12}}$ taken from [15]. The upper figure shows a relativistic calculation while the lower figure shows a non relativistic one. p Ge states are the dominating contribution at the Fermi level

2.3. Transport phenomena

2.3.1. Boltzmann equation

[8] In order to describe a gas of N equal particles a probability distribution function $\mathrm{f}(\tilde{\mathrm{r}}, \tilde{\mathrm{k}}, \mathrm{t})$ for one particle is used. $\mathrm{f}(\tilde{\mathrm{r}}, \tilde{\mathrm{k}}, \mathrm{t})\mathrm{d}^3\mathrm{r}\mathrm{d}^3\mathrm{k}$ is the number of particles in the phase space volume $\mathrm{d}^3\mathrm{r}\mathrm{d}^3\mathrm{k}$. For metallic materials heat and charge transport is mainly performed by electrons. So in this case $\mathrm{f}_0(\tilde{\mathrm{r}}, \tilde{\mathrm{k}}, \mathrm{t})$, the equilibrium probability distribution function is the Fermi-Dirac equation.

$$f_0(E(\vec{k})) = \frac{1}{1 + \exp\frac{E(\vec{k})-\mu}{k_B T}} \tag{2.12}$$

Transport means having a non equilibrium state. In order to get the Boltzmann transport equation we have to consider forces that give electrons a reason to move ($\Delta T, \vec{E}, \vec{B}$) and developing over the time dt.

$$f(\vec{r} + \dot{\vec{r}}dt, \vec{k} + \dot{\vec{k}}dt, t + dt) - f(\vec{r}, \vec{k}, t) = 0 \tag{2.13}$$

Without scattering processes we get Eqn. 2.13, called Liouville´s equation. This equation says that, the distribution function stays constant while following a path in the phase space in time and is valid for conservative systems. The number of particles in the phase space volume $\mathrm{d}^3\mathrm{r}\mathrm{d}^3\mathrm{k}$ is equal to the number of particles in $\mathrm{d}^3(\mathrm{r} + \mathrm{vt})\mathrm{d}^3(\mathrm{k} + (\mathrm{F}/\hbar)\mathrm{dt})$.

$$\left(\frac{\partial}{\partial t} + \dot{\vec{k}}\nabla_{\vec{k}} + \dot{\vec{r}}\nabla_{\vec{r}}\right) f(\vec{r}, \vec{k}, t) = 0 \tag{2.14}$$

Development in a Taylor series and considering only first order terms leads to Eqn. 2.14.

$$\left(\frac{\partial}{\partial t} + \dot{\vec{k}}\nabla_{\vec{k}} + \dot{\vec{r}}\nabla_{\vec{r}}\right) f(\vec{r}, \vec{k}, t) = \left(\frac{\partial f}{\partial t}\right)_{coll} \tag{2.15}$$

Now considering besides the external forces also scattering processes, the equation ends up in Eqn. 2.15. Particles are scattered into or out of the phase space volume elements $\mathrm{d}^3\mathrm{r}\mathrm{d}^3\mathrm{k}$, $\mathrm{d}^3(\mathrm{r} + \mathrm{vdt})\mathrm{d}^3(\mathrm{k} + (\mathrm{F}/\hbar)\mathrm{dt})$.

$$\frac{\partial f}{\partial t} = -\vec{v}\nabla_{\vec{r}} f - \frac{e}{\hbar}\left(\vec{E} + \vec{v} \times \vec{B}\right)\nabla_{\vec{k}} f + \left(\frac{\partial f}{\partial t}\right)_{coll} \tag{2.16}$$

[8] From references [18], [19], [20] and [21]

Using $\frac{\partial \tilde{\mathrm{k}}}{\partial \mathrm{t}} = \frac{\tilde{\mathrm{F}}}{\hbar} = \frac{\mathrm{e}}{\hbar}\left(\tilde{\mathrm{E}} + \tilde{\mathrm{v}} \times \tilde{\mathrm{B}}\right)$ and $\frac{\partial \tilde{\mathrm{r}}}{\partial \mathrm{t}} = \tilde{\mathrm{v}}$ leads to Eqn. 2.16, the Boltzmann equation. The first term of the right side of Eqn. 2.16 stands for diffusion and the second is the result of external forces. In stationary case $\frac{\partial \mathrm{f}}{\partial \mathrm{t}} = 0$ this two terms have to be balanced by the scattering term. Generally, this scattering term is described with the probability of a particle changing from a quantum state k to k' $\mathrm{P_{k,k'}} \propto \langle \mathrm{k'} | \mathrm{H} | \mathrm{k} \rangle$. The relaxation time approach 2.17 for the scattering terms is based on the idea that the difference between the static distribution $\mathrm{f_0}$ and f decays exponentially with the relaxation time τ.

$$\left(\frac{\partial f}{\partial t}\right)_{coll} = \frac{f - f_0}{\tau} \tag{2.17}$$

For the case of stationary forces $\frac{\partial \mathrm{f}}{\partial \mathrm{t}}$ in Eqn. 2.16 is neglected.

$$\frac{f - f_0}{\tau} = \vec{v}\nabla_{\vec{r}} f + \frac{e}{\hbar}\vec{E}\nabla_{\vec{k}} f \tag{2.18}$$

Considering a temperature gradient in the Fermi Dirac distribution:

$$f_0(\vec{k}) \Rightarrow f_0(\vec{k}, \vec{r}) = \frac{1}{\exp \frac{\epsilon(\vec{k}) - \mu}{k_B T(\vec{r})} + 1} \tag{2.19}$$

For small differences from equilibrium state $\tilde{\mathrm{v}}(\tilde{\mathrm{k}})\nabla_{\tilde{\mathrm{r}}}\mathrm{f}(\tilde{\mathrm{k}}, \tilde{\mathrm{r}}) \cong \tilde{\mathrm{v}}(\tilde{\mathrm{k}})\nabla_{\tilde{\mathrm{r}}}\mathrm{f_0}(\tilde{\mathrm{k}}, \tilde{\mathrm{r}})$ and $\tilde{\mathrm{E}}(\mathrm{k})\nabla_{\tilde{\mathrm{k}}}\mathrm{f}(\tilde{\mathrm{k}}, \tilde{\mathrm{r}}) \cong \tilde{\mathrm{E}}(\mathrm{k})\nabla_{\tilde{\mathrm{k}}}\mathrm{f_0}(\tilde{\mathrm{k}}, \tilde{\mathrm{r}})$, see [22], and the relations 2.20, 2.21 and 2.22 we get a simplified Boltzmann equation, Eqn. 2.23.

$$\nabla_k f_0 = \frac{\partial f_0}{\partial \epsilon}\nabla_k \epsilon = \frac{\partial f_0}{\partial \epsilon}\hbar\vec{v}(\vec{k}) \tag{2.20}$$

$$\nabla_{\vec{r}} f_0(\vec{k}, \vec{r}) = \frac{\partial f_0}{\partial T}\nabla_{\vec{r}} T \tag{2.21}$$

$$\frac{\partial f_0}{\partial T} = -\left(\frac{\epsilon - \mu}{T}\right)\frac{\partial f_0}{\partial \epsilon} \tag{2.22}$$

$$\frac{f - f_0}{\tau} = \left[-eE + \frac{(\epsilon - \mu)}{T}\nabla_{\vec{r}} T\right]\vec{v}_{\vec{k}}\frac{\partial f_0}{\partial \epsilon} \tag{2.23}$$

For small differences from the equilibrium state $\mathrm{g}(\tilde{\mathrm{k}}) = \mathrm{f}(\tilde{\mathrm{k}}) - \mathrm{f_0}(\tilde{\mathrm{k}})$ the linearized Boltzmann equation, Eqn. 2.23 is derived, in order to have an expression of $\mathrm{f}(\tilde{\mathrm{k}})$, only depending on first order terms $\mathrm{f_0}(\tilde{\mathrm{k}})$. The transport integrals are derived for the case B=0, starting with Eqn. 2.18.

2.3.2. Transport integrals

[9] The simplification of the Boltzmann equation finally is an expression for $\mathrm{f}(\tilde{\mathrm{k}}, \tilde{\mathrm{r}})$ depending on first order deviations of f_0.

$$f(\vec{k}, \vec{r}) = f_0(\vec{k}) - \tau \left[eE - \frac{(\epsilon - \mu)}{T} \nabla_{\vec{r}} T \right] \vec{v}_{\vec{k}} \frac{\partial f_0}{\partial \epsilon} \tag{2.24}$$

The definition of heat the current from a microscopic point of view is the sum of the energy $(\epsilon - \mu)$ transported with the velocity $\tilde{\mathrm{v}}$ over all particles.

$$\vec{q} = \frac{V}{4\pi^3} \int (\epsilon - \mu) \vec{v}_r f(\vec{k}, \vec{r}) d^3k \tag{2.25}$$

Similarly, the electrical current can be defined as the sum of the electric charge transported from all particles.

$$\vec{j} = \frac{V}{4\pi^3} \int e \vec{v}_r f(\vec{k}, \vec{r}) d^3k \tag{2.26}$$

Combining Eqn. 2.25 and 2.26 with 2.24 gives the microscopic expressions for heat and electrical current.

$$\vec{q} = \frac{Ve}{4\pi^3} \int \vec{v}_r \vec{v}_r (\epsilon - \mu) \tau \left(-\frac{\partial f_0}{\partial \epsilon} \right) \vec{E} d^3k - \frac{V}{4\pi^3 T} \int \vec{v}_r \vec{v}_r (\epsilon - \mu)^2 \tau \left(-\frac{\partial f_0}{\partial \epsilon} \right) \nabla_{\vec{r}} T d^3k \tag{2.27}$$

$$\vec{j} = \frac{Ve^2}{4\pi^3} \int \vec{v}_r \vec{v}_r \tau \left(-\frac{\partial f_0}{\partial \epsilon} \right) \vec{E} d^3k - \frac{Ve}{4\pi^3 T} \int \vec{v}_r \vec{v}_r (\epsilon - \mu) \tau \left(-\frac{\partial f_0}{\partial \epsilon} \right) \nabla_{\vec{r}} T d^3k \tag{2.28}$$

In order to simplify and find the connection to the macroscopic equations transport integrals are defined with:

$$K_n = \frac{V}{4\pi^3} \int \vec{v}_r \vec{v}_r \tau (\epsilon - \mu)^n \left(-\frac{\partial f_0}{\partial \epsilon} \right) d^3k \tag{2.29}$$

what ends in two short equations for $\tilde{\mathrm{q}}$ and $\tilde{\mathrm{j}}$.

$$\vec{q} = eK_1 \vec{E} - \frac{1}{T} K_2 \nabla_{\vec{r}} T \tag{2.30}$$

$$\vec{j} = e^2 K_0 \vec{E} - \frac{e}{T} K_1 \nabla_{\vec{r}} T \tag{2.31}$$

Using border conditions macroscopic transport quantities (electrical resistivity, thermal conductivity, thermopower) are derived.

[9] From references [23], [13], [24], [22] and [21]

2.3.3. Electrical resistivity

[10] ρ is defined as inverse proportionality factor of current density and field strength $\tilde{\mathrm{E}}$. ρ is tensor in non-isotropic media. Assuming the typical border conditions for measuring: $\tilde{\mathrm{E}} \neq 0, \nabla_{\tilde{\mathrm{r}}}\mathrm{T} = 0, \tilde{\mathrm{B}} = 0$, and using Eqn. 2.31 leads to the current density:

$$\vec{j} = e^2 K_0 \vec{E} = \rho^{-1}\vec{E} \tag{2.32}$$

$$\rho^{-1} = e^2 K_0 \tag{2.33}$$

Solving the transport integral K_0, assuming an isotropic medium and free electrons (see reference [25], page 102,103) Eqn. 2.34 is achieved. This equation looks very similar to the semi- classical Drude model, with $\tau(\mathrm{E_F})$, indicating that only the electrons on the Fermi surface participate in conduction and m^* the effective mass instead of the electron mass.

$$\rho^{-1} = \frac{e^2\tau(E_F)}{m^*}n \tag{2.34}$$

Searching a model for the temperature dependence of the resistivity it is important considering the different causes of resistivity. The strongest impact on resistivity at high temperature in metals is the electron- phonon scattering. Other sources derive from lattice imperfections or impurities and are here considered as temperature independent. Other scattering terms might come from electron electron scattering (for low temperatures) or magnetic moments. The very important Matthiessen rule assumes that scattering processes are independent and so the inverse relaxation times can be added.

$$\frac{1}{\tau} = \sum \frac{1}{\tau_i} \tag{2.35}$$

Bloch- Grüneisen- model

The Bloch-Grüneisen equation is an equation that describes the electron- phonon scattering and the resulting resistivity. Its a variation type calculation of lowest order based on a spherical free electron band structure and a spherical Debye phonon spectrum of a single longitudinal branch.

$$\rho(T) = \rho_0 + c_2\Theta_D\left(\frac{T}{\Theta_D}\right)^5 \int_0^{\Theta_D/T} \frac{z^5 dz}{(\exp z - 1)(1 - \exp -z)} \tag{2.36}$$

[10] From references [22], [25] and [26]

For high temperatures ($T >> \Theta_D$) the Bloch- Grüneisen term is proportional to the temperature. For low temperatures $\rho_{\mathrm{ph}} \propto \mathrm{T}^5$.

2.3.4. Thermal conductivity

[11] The macroscopic law of heat conduction, the Fourier law, states that the time rate of heat transfer through a material is proportional to the negative temperature gradient.

$$\vec{q} = -\lambda \nabla_{\vec{r}} T \tag{2.37}$$

measuring border conditions: $\tilde{\mathrm{j}} = 0, \nabla_{\tilde{\mathrm{r}}}\mathrm{T} \neq 0, \tilde{\mathrm{B}} = 0$ used in Eqn. 2.31 gives an expression for the electric field:

$$\vec{E} = \frac{K_1}{eTK_0} \nabla_{\vec{r}} T \tag{2.38}$$

Now combining with Eqn. 2.30

$$\vec{q} = eK_1 \frac{K_1}{eTK_0} \nabla_{\vec{r}} T - \frac{1}{T} K_2 \nabla_{\vec{r}} T = -\frac{1}{T} \left(K_2 - \frac{K_1^2}{K_0} \right) \nabla_{\vec{r}} T \equiv \lambda \nabla_{\vec{r}} T \tag{2.39}$$

$$\lambda = -\frac{1}{T} \left(K_2 - \frac{K_1^2}{K_0} \right) \tag{2.40}$$

In order to find a model that describes the temperature dependence of the thermal conductivity we consider the thermal conductivity λ as a sum of the electronic contribution λ_{el} and the lattice contribution λ_{l}. The electronic contribution is, like the resistivity, influenced by interactions of the electrons with static imperfections and interactions with phonons. For metals this λ_{el} is connected with the resistivity with the Wiedemann Franz law.

$$\lambda_{el} = \frac{L_0 t}{\rho} \tag{2.41}$$

The Lorenz number L_0 is $2.45 * 10^{-8} \mathrm{W}\Omega/\mathrm{K}^2$. The phonon contribution can be described by the Callaway model, explained in detail in reference [27]. The Callaway model uses Debye phonon distribution and is approximated with $\mathrm{v_s} = \frac{\mathrm{k_B}\Theta_\mathrm{D}}{\hbar(6\pi^2\mathrm{n})^{1/3}}$ and $\mathrm{x} = \hbar/\mathrm{k_B T}$ by:

$$\lambda_l = \frac{k_B}{2\pi^2 v_s} \left(\frac{k_b}{\hbar} \right)^3 T^3 \int_0^{\frac{\Theta_D}{T}} \frac{\tau_C x^4 e^x}{\left(e^x - 1\right)^2} dx \tag{2.42}$$

[11] From references [22], [27] and [21]

This model uses Matthissen rule and sums over the relaxation times of different scattering events.

$$\frac{1}{\tau_C} = \frac{1}{\tau_U} + \frac{1}{\tau_D} + \frac{1}{\tau_B} + \frac{1}{\tau_{el-ph}} \tag{2.43}$$

The considered scattering mechanism are: Umklapp processes τ_{U}, defect scattering τ_{D}, boundary scattering τ_{B} and electron- phonon scattering $\tau_{\mathrm{el-ph}}$, see reference [21].

$$\begin{aligned} \frac{1}{\tau_U} &\propto T^3 x^2 e^{\frac{-\Theta_D}{2T}} \\ \frac{1}{\tau_D} &\propto x^4 T^4 \\ \frac{1}{\tau_B} &\propto const \\ \frac{1}{\tau_{el-ph}} &\propto Tx. \end{aligned} \tag{2.44}$$

2.3.5. Thermopower

[12] The thermopower (thermoelectric power, Seebeck effect) of a material is the induced thermoelectric voltage in response to a temperature difference across that material.

$$\vec{E} = S\nabla_{\vec{r}} T \tag{2.45}$$

The measurement border conditions are, like for thermal conductivity, $\tilde{\mathrm{j}} = 0, \nabla_{\tilde{\mathrm{r}}}\mathrm{T} \neq 0, \tilde{\mathrm{B}} = 0$, so we use Eqn. 2.38 and compare with the definition of the Seebeck coefficient:

$$\vec{E} = -\frac{K_1}{eTK_0}\nabla_{\vec{r}} T = S\nabla_{\vec{r}} T \tag{2.46}$$

$$S = -\frac{K_1}{eTK_0} \tag{2.47}$$

2.3.6. ZT figure of merit

[13] In order to compare the thermoelectric properties of new materials it is important to have a value that compares the efficiency in therms of material properties, not of impacts like the temperature difference, size of the device or the resistivity of the user. This value is the dimensionless quantity ZT. It is defined in Eqn. 2.8. The connection between ZT

[12] From reference [22]
[13] From reference [28]

and efficiency is (approximated by neglecting the losses of Joule heating):

$$\mu = \frac{W}{Q} = \frac{T_1 - T_0}{T_1} \frac{\sqrt{1 + \frac{Z}{2}(T_1 - T_0)} - 1}{\sqrt{1 + \frac{Z}{2}(T_1 - T_0)} + \frac{T_0}{T_1}} \tag{2.48}$$

The left part is the definition of the efficiency with W, the provided electric power divided by used thermal energy Q provided by the heat source. The right part consists of the Carnot efficiency multiplied by a a part that includes Z, the material specific properties.

2.3.7. Charge carrier density - Hall effect

[14] The Hall effect can be used to measure the charge carrier density. This is done by using a magnetic field $\mathrm{B_z}$ and an electric field $\mathrm{E_x}$, applied perpendicular. Due to the Lorentz force there will also be a current in a right angle to the surface of magnetic- and electric field vector. For only one type of charge carrier (electrons or holes) the charge carrier concentration can be determined as follows:

$$E_y = -\frac{e\tau}{m} E_x B_z \tag{2.49}$$

Using $\mathrm{j} = \frac{\mathrm{ne^2 \tau E_x}}{\mathrm{m}}$, $\mathrm{R_H}$ is defined as

$$R_H = \frac{E_y}{j_x B_z} = -\frac{1}{ne} \tag{2.50}$$

With $\mathrm{E_y}$ the resulting field due to Lorenz force, $\mathrm{R_H}$ the hall constant and n the charge carrier density.

2.4. Heat capacity

[15] The specific heat capacity is the amount of heat required to increase the temperature of a specified amount of solid by one Kelvin. The amount of solid can be specified by weight or mol. Heat can be stored by electrons, by lattice vibrations, and by all particles and quasi particles one can think of. Assuming this contributions as independent we start with Eqn. 2.51:

$$C(T) = C_{el} + C_p + C_{mag} + C_{nuc} \tag{2.51}$$

[14] From reference [24]
[15] From references [6] and [18]

With the specific heat expressed in state variables

$$C_V = T\left(\frac{\partial S}{\partial T}\right)_V = \frac{\partial U}{\partial T}_{V,N} \tag{2.52}$$

$$C_p = T\left(\frac{\partial S}{\partial T}\right)_p = \frac{\partial H}{\partial T}_{V,N} \tag{2.53}$$

and the internal energy defined as the integral over the spectral density of the internal energy, depending of the energy ϵ, the density of states at this energy $\mathrm{D}(\epsilon)$ and the occupation distribution function $\mathrm{f}(\epsilon)$.

$$U = \sum_{ks} \epsilon(ks) f(\epsilon(ks), T) = \int \epsilon D(\epsilon) f(\epsilon) d\epsilon \tag{2.54}$$

2.4.1. Electronic contribution

[16] The specific heat for free electrons is proportional to T, see Eqn.2.55. A qualitative understanding can be gained by the following assumptions: Not all electrons N can absorb thermal energy, only the ones in the region of ϵ_F. The size of this region increases with temperature because the Fermi function smears out with increasing temperature and therefore there are free possible states in a broader energy region that can participate. So the amount of electrons that give contribution to the heat capacity is the $\frac{\mathrm{T}}{\mathrm{T_F}}$ th part of all N electrons. Each one of these electrons has a thermal energy of $\mathrm{k_B T}$, so the internal energy is proportional to $\mathrm{U} \propto \frac{\mathrm{NT}}{\mathrm{T_F}} \mathrm{k_B T}$ and the specific heat to $\mathrm{C_{el}} = \frac{\partial \mathrm{U}}{\partial \mathrm{T}} \propto 2\mathrm{N k_B} \frac{\mathrm{T}}{\mathrm{T_F}}$. A proper derivation, see reference [24] gives 2.55.

$$C_{el} = \frac{1}{3}\pi^2 D(\epsilon_F) k_B^2 T = \frac{1}{2}\pi^2 N k_B \frac{T}{T_F} \tag{2.55}$$

2.4.2. Contribution of the lattice

[17] Using Eqn. 2.54, the expression for the internal energy of phonons, summed over all polarisations p:

$$U = \sum_p \int \frac{\hbar\omega}{\exp\frac{\hbar\omega}{k_B T} - 1} D(\omega) d\omega \tag{2.56}$$

[16] From reference [24]
[17] From references [25] and [29]

With Eqn. 2.52 we get an expression for the specific heat:

$$C_{V,latt} = k_B \sum_p \int D(\omega) \frac{\left(\frac{\hbar\omega}{k_B T}\right)^2 \exp \frac{\hbar\omega}{k_B T}}{\left(\exp \frac{\hbar\omega}{k_B T} - 1\right)^2} d\omega \tag{2.57}$$

Now we still need a model for $\mathrm{D}(\omega)$.

Einstein model

The Einstein model uses a phonon density of states according to:

$$D(\omega) = N\delta(\omega - \omega_0) \tag{2.58}$$

with Eqn. 2.57 the specific heat ends up in

$$C_{V,latt} = 3k_B N \frac{\left(\frac{\hbar\omega}{k_B T}\right)^2 \exp \frac{\hbar\omega}{k_B T}}{\left(\exp \frac{\hbar\omega}{k_B T} - 1\right)^2} \tag{2.59}$$

Debye model

In this model the phonon density of states increases like ω^2 until the the so called Debye-frequency and is zero above this Debye frequency. Similar to the Fermi level, the cut-off is chosen such that the total number of states is 3N ($3N = \int_0^{\omega_D} D(\omega) d\omega$.

$$D(\omega) = \frac{3V\omega^2}{2\pi^2 c^3} = \frac{9N\omega^2}{\omega_D^3} \tag{2.60}$$

Eqn. 2.60 assumes a linear dispersions relation with c, the speed of sound and the Volume $\mathrm{L}^3 = \mathrm{V}$. The integral runs from $\omega = 0$ to $\omega = \omega_\mathrm{D}$.

$$C_{V,latt} = \frac{9N}{\omega_D^3} \int_0^{\omega_D} \frac{\left(\frac{\hbar\omega}{k_B T}\right)^2 \exp \frac{\hbar\omega}{k_B T}}{\left(\exp \frac{\hbar\omega}{k_B T} - 1\right)^2} \omega^2 d\omega \tag{2.61}$$

Later $\mathrm{C_V}$ is used, normed per mol, so the equation we use for fitting and extracting the Debye temperature is the following:

$$C_{V,latt} = 9Rn \left(\frac{T}{\Theta_D}\right)^3 \int_0^{x_D} \left(\frac{x^4 e^x}{(e^x - 1)^2}\right) \tag{2.62}$$

with n the number of atoms per formula unit and $\mathrm{R} = \mathrm{k_B} * \mathrm{N_A}$, R gas constant, $\mathrm{k_B}$ Boltzmann constant and $\mathrm{N_A}$ the Avogadro constant. For low temperatures ω_D is substituted with ∞ and we get the famous T^3 Debye law, with $\frac{\hbar\omega_\mathrm{D}}{\mathrm{k_B T}} = \frac{\Theta_\mathrm{D}}{\mathrm{T}}$:

$$C_{V,latt} = \frac{12\pi^4}{5} Rn \left(\frac{T}{\Theta_D}\right)^3 = \beta T^3 \tag{2.63}$$

while for high temperatures we end up in the classical law from Dulong- Petite: $\mathrm{C_V} = 3\mathrm{R}$. The Debye Model only cares about the acoustic branches (linear dispersions relation approximation) where all three branches are replaced by one intermediate. For lattices with a base of more than one atom there are three acoustic and 3p-3 optic branches. A model for $\mathrm{D}(\omega)$ is then:

$$D(\omega) = N \left(\frac{9\omega^2}{\omega_D^3} + \sum_{i=1}^{3p-3} \delta(\omega - (\omega_E)_i)\right) \tag{2.64}$$

2.5. Thermal expansion

[18] Thermal expansion is described by the relative length change of the sample coming from the change of particle displacement with the temperature.

$$\Delta l / l(T_0) = \frac{\langle x \rangle_T - \langle x \rangle_{T_0}}{x_0} \tag{2.65}$$

Thermal expansion is a phenomenon that can be described with the help of anharmonic contributions to the internal energy of phonons. The potential, before described with a quadratic term of the particle displacement (harmonic oscillator) is now extended by a x^3 and x^4 term. Physically, the first term should describe the asymmetry of repulsive forces between the ions and the second term describes a weakening of the potential for large Amplitudes.

2.5.1. Model debye einstein approach

[19] Eqn. 2.66 is the potential energy (including anharmonic terms) with respect to the particle displacement x.

$$U(x) = cx^2 - gx^3 - fx^4 \tag{2.66}$$

[18] From references [30], [24], [31] and [32]
[19] From references [31] and [24]

In order to calculate the average lattice displacement depending on temperature, we use the Boltzmann distribution:

$$\langle x \rangle_T = \frac{\int_{\infty}^{-\infty} x \exp^{-\beta U(x)}}{\int_{\infty}^{-\infty} \exp^{-\beta U(x)}} \tag{2.67}$$

Solving this equation, neglecting terms higher T^3 Eqn. 2.68 is gained, with $\mathrm{G} = \frac{15}{16}\frac{\mathrm{g}^2}{\mathrm{c}^3} - \frac{8\mathrm{f}}{\mathrm{c}^2}$ and $\mathrm{F} = \frac{35}{16}\left(\frac{15}{4}\frac{\mathrm{g}^2\mathrm{f}}{\mathrm{c}^5} - \frac{3\mathrm{f}^2}{\mathrm{c}^4}\right)$.

$$\langle x \rangle_T = \frac{3g}{4c^2}(k_B T)[1 - G(k_B T) - F(k_B T)^2] \tag{2.68}$$

For some reason the thermal energy $\mathrm{k_B T}$ is now expressed with the internal energy of the lattice (including Debye and Einstein modes). Furthermore a T^2 part is added in order to consider the influence of free electrons.

$$\langle x \rangle_T = \frac{3g}{4c^2}[\epsilon - G\epsilon^2 - F\epsilon^3] \tag{2.69}$$

with ϵ the internal energy of the phonons:

$$\epsilon = \left\{ \left(\frac{3}{p}\right) 3k_B T \left(\frac{T}{\Theta_D}\right)^3 \int_0^{\Theta_D/T} \frac{z^3 dz}{exp^z - 1} + \left(\frac{p-3}{p}\right) \frac{k_B \Theta_E}{exp^{\Theta_E/T} - 1} \right\} \tag{2.70}$$

2.5.2. Grüneisen-parameter

[20] Thermodynamic assumptions lead to the Grüneisen- parameter. The coefficient of thermal expansion is defined as the degree of expansion divided by the change in temperature. Using the definition of the bulk modulus $\mathrm{B} = -\mathrm{V}\left(\frac{\partial \mathrm{P}}{\partial \mathrm{V}}\right)_{\mathrm{T}}$, we obtain α in dependence of the pressure.

$$\alpha = \frac{1}{3V}\left(\frac{\partial V}{\partial T}\right)_P = \frac{1}{3B}\left(\frac{\partial P}{\partial T}\right)_V = \frac{1}{l}\left(\frac{\partial l}{\partial T}\right)_P \tag{2.71}$$

Now we express the pressure in terms of the internal energy:

$$P = -\left(\frac{\partial U}{\partial V}\right)_S \tag{2.72}$$

[20] From reference [32]

The internal energy in Eqn. 2.54 can now be used to express α in terms of energy/frequency. Considering Eqn. 2.52, $\mathrm{C_V}$ is also expressed by the internal energy. Eqn. 2.73 and 2.74 shall point out the similarity of these two measurable values.

$$\alpha = \frac{1}{3B} \sum_{ks} \frac{\partial}{\partial V} \hbar\omega_{ks} \frac{\partial}{\partial T} f(\omega_{ks}, T) \tag{2.73}$$

$$C_V = \sum_{ks} \frac{\hbar\omega_{ks}}{V} \frac{\partial}{\partial T} f(\omega_{ks}, T) \tag{2.74}$$

Using the Bose Einstein distribution $\mathrm{f}(\omega_{\mathrm{ks}}, \mathrm{T}) = \frac{1}{\exp^{\beta\hbar\omega_{\mathrm{ks}}} - 1}$ and considering each mode k, s separately, the Grueneisen- parameter is microscopic defined as

$$\Gamma_{ks} = -\frac{V}{\omega_{ks}} \frac{\partial \omega_{ks}}{\partial V} = -\frac{\partial(ln(\omega_{ks}))}{\partial(ln(V))} \tag{2.75}$$

and connected with the macroscopic world by Eqn. 2.76 and 2.77.

$$\Gamma = -\frac{\sum_{ks} \Gamma_{ks} C_{Vks}}{\sum_{ks} C_{Vks}} \tag{2.76}$$

$$\alpha = \frac{\Gamma C_V}{B} \tag{2.77}$$

3. Experimental design

Two sample series ($LaPt_4Ge_{12-x}Sb_x$ x = 0, 1, 2, 3, 4, 5, 5.1, 6, 7 and $BaPt_{(4-x)}Ir_xGe_{12}$ x = 1, 2, 3, 4) were produced and analyzed with respect to physical and chemical properties.

3.1. Sample preparation

Samples with a mass of 1-1.5 g were prepared by arc melting of the pure elements in argon atmosphere and annealing afterwards. The loose of weight of La and Ba was corrected by using 2 weight % more La/Ba. The standard annealing temperature was 800°C for 10 days, but there were also made experiments at 750°C and 900°C in order to improve the solubility. Samples were sealed in quarz tubes for annealing and quenched afterwards in water. As the $LaPt_4Ge_{12-x}Sb_x$ series samples were very brittle, one ball milled and hot pressed sample was produced with the nominal composition $LaPt_4Ge_8Sb_4$. This was done by three arc melted samples ball milled in a Vario Planetenmühle, Pulverisette 4 (ball milling in argon athmosphere). Inside a glovebox the nanosized powder was filled into a cylinder with a diameter of 10mm. A hot press HP W 200/250-2200-200-KS (FCT Systeme GmbH) was used for hot pressing samples for 30min at 700°C. For more details see reference [33].

3.2. Structure analysis

[1] All samples were analyzed, in as cast condition as well as annealed, by X-ray powder diffraction at room temperature using pulverized samples. Using monochromatic $CuK_\alpha 1$ radiation (λ = 0.154051 nm) and a Huber Guinier detection system imaging plate it is a powerful tool to identify phases. Using pure silicon as internal standard (lattice parameter 5.43095 $\mathring{A}$ at RT) lattice parameters were calculated by least squares approximation

[1] From reference [30]

of elected peaks. Rietveld refinement of the crystal structures was made for all the samples, using the program FullProf. All dense and not too brittle samples (as cast condition/annealed) were embedded, polished and viewed in the electron microscope. Energy dispersive X-ray analysis (EDX) was used to identify the phases observed in the backscattered electrons (BSE) scanning picture. Combination of the EDX measurement and X-ray is used to identify the phases.

3.3. Heat capacity

[2] Heat capacity was measured using a quasi adiabatic step heating technique. The device used is typical for the quasi adiabatic Nernst technique and described in [35]. The used samples had a weight of $0.8 - 1.2$ g and were measured from 2.6 to 300 K.

3.4. Thermal expansion

A miniature capacitance dilatometer was used to measure the thermal expansion. This equipment is very well described in [36]. It is important to perform the measurement with a dense, plane sample.

3.5. Magnetic properties

Magnetic measurements were carried out by a SQUID-magnetometer (Cryogenics Magnetometer S603) in a temperature range from 2-300 K. The sample masses were about 20 mg; shape does not matter, thats why it was a good technique to gain at least some information of the brittle samples. The measurements were performed in a dc field. Field cooling and zero field cooling method were used. Field cooling means that the field is applied above the transition temperature and while cooling down magnetization measurement is done. Zero field measurement is done by cooling down the sample without a field, then apply a field and measure while warming up.

[2] From references [34] and [35]

3.6. Resistivity

The samples analyzed were bar- shaped, with a length of 7-9 mm, and a squared cross section with a width of 1.3 mm. Low temperature measurements (4-300 K) were performed with a home-made standard four-terminal AC and DC measuring technique, using four gold needles to perform the contact with the sample. The whole assembly is inserted in a He4 bath. For further details see [23]. Measurements from room temperature upwards were done by an ULVAC RIKO ZEM-3 equipment, which simultaneously also measures the Seebeck coefficient. More detailed description on this instrument can be found in [30].

3.7. Seebeck coefficient

Below room temperature the thermopower was measured with a home- made device which heats samples in AC mode. The tools main parts are two strain gauge, that produces, because of the resistivity a very defined amount of heat, and two thermocouples to measure the temperatures, as well as the voltage between the two sides. The same bar shaped samples from the resistivity measurements were used. In order to have better contacts with the thermocouple the sites where the contacts were going to be fixed with silver conductive paste, has been sputtered with a layer of gold/palladium.

3.8. Thermal conductivity

Thermal conductivity was measured for the one hot pressed sample by steady state heat flow method in a flow cryostat. The sample used had a size of 1.6 x 1 x 8 mm. It is thermally contacted on two sites (4.44 mm distance) with fine copper wires, which are connected with thermocouples. A defined heat flow is provided by a strain gauge and a copper heat sink, that is connected to the helium flow heat exchanger. The most challenging part of this measurement is to get a stable heat flow in thermoelectric materials, which have a small thermal conductivity. The sample and its connections are surrounded by three radiation shields. Still above 150K radiation losses have to be considered as an additional term T^3.

3.9. Hall measurement

Hall measurement was performed with a Physical Property Measurement System (PPMS).

3.10. Errors

Generally the errors made are relativly small. A cursory error estimation for temperatures below 20 K: 3% for the low temperature Seebeck measurement, 5% for the thermal conductivity measurement, 1% for the low temperature resistivity measurement and less than 1% for the heat capacity measurement.

4. Results and analyses

4.1. Sample preparation and analyses

4.1.1. $LaPt_4Ge_{12-x}Sb_x$-system

Different samples of the $LaPt_4Ge_{12-x}Sb_x$-system were produced, starting from a reference sample without Sb until the end of the solubility. All samples were measured with X-ray powder diffraction and analyzed in the electron microscope, making energy-dispersive X-ray micro probe analysis of all different recognized phases. Table A.1 shows a summary of this measurements. The X-ray powder diffraction patterns proved the structure type $LaFe_4P_{12}$, space group $Im\bar{3}$. The lattice parameter of the skutterudite increases with the amount of solved Sb (figure 4.6(b)). A linear fit of this dependence gives the equation $y = 0.0558x + 8.6278$. Fig. 4.1 shows a X-ray powder diffractogramm of the reference sample and the sample with $x = 5.1Sb$ content. As the lattice parameter is getting larger the peaks in Fig. 4.1 shift to the left. Furthermore the relative height of the peaks changes due to different electron densities of the substituted atoms. The end of the solubility was reached at about $x = 5.1$ at 800°C, see Fig. 4.6(a), where the filled circles are the lattice parameters and the unfilled circles are the EDX measured Sb contents of the different samples. The samples were partially very brittle, see Fig. A, so not all physical properties could be measured. Due to the annealing process quite pure samples could be produced containing the $LaPt_4Ge_{12-x}Sb_x$ skutterudite and small impurities of Ge or $LaPt_2Ge_2$. In order to increase the solubility, annealing at a higher Temperature (910°C) was tried, however without success. The Sb content solved was about $x = 4.9$. Fig. 4.5 shows a differential scanning calorimetry measurement, finding the melting point of the skutterudites around 942°C. Fig. 4.4 shows the unit cell of the sample with the nominal composition $LaPt_4Ge_7Sb_5$, gained from the Rietveld refinement of the powder pattern, Fig. 4.2.

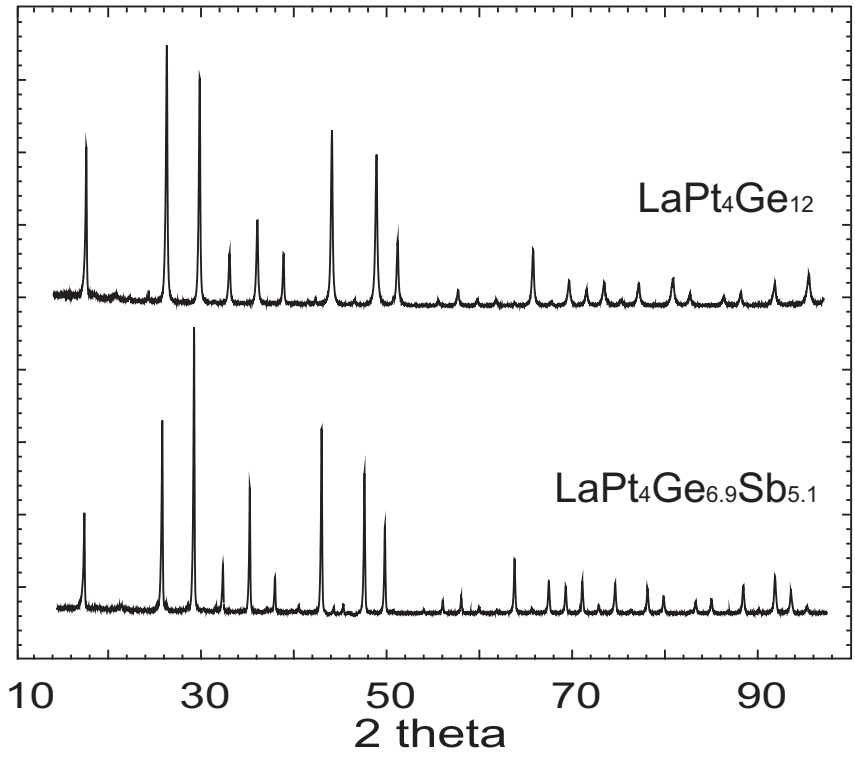

Figure 4.1.: comparison of the powder diffractogramm of the Reference sample $LaPt_4Ge_{12}$ and $LaPt_4Ge_{6.9}Sb_{5.1}$

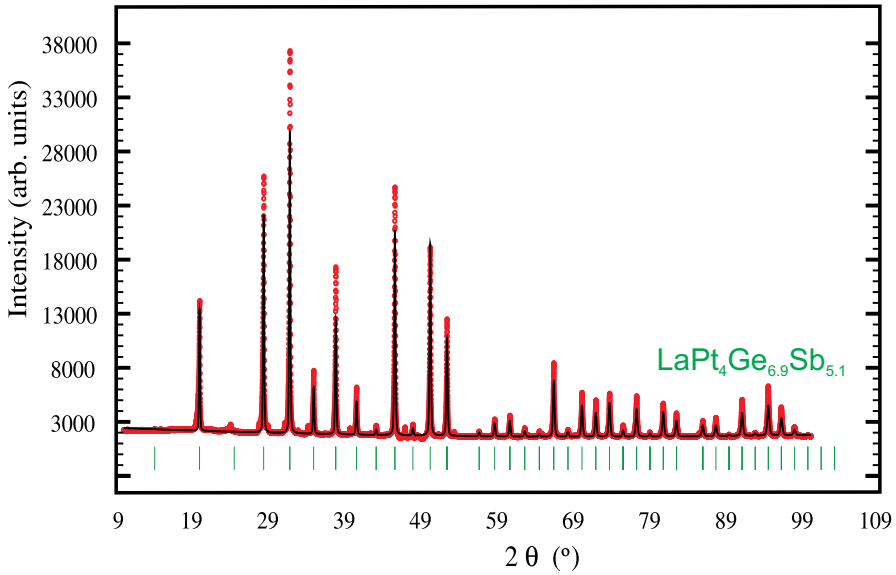

Figure 4.2.: Rietveld refinement for the sample with nominal composition $LaPt_4Ge_7Sb_5$

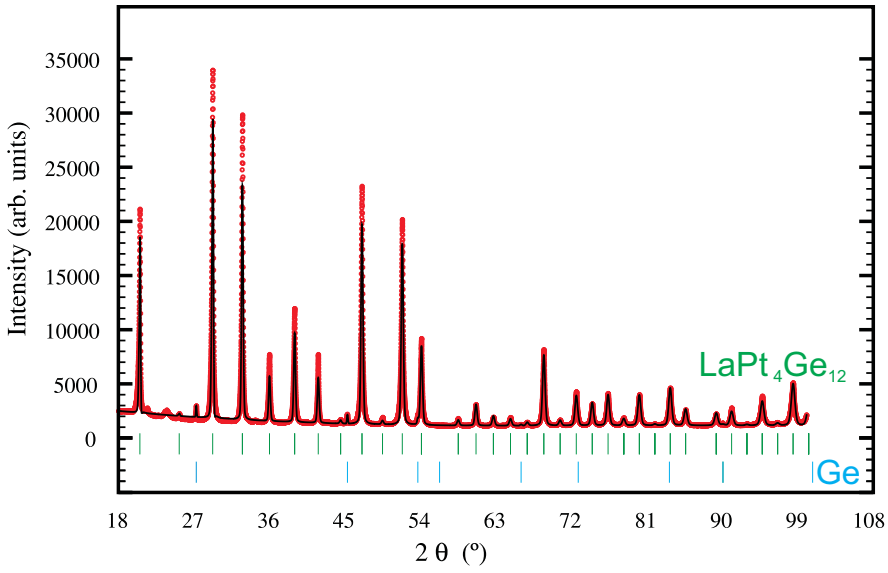

Figure 4.3.: Rietveld refinement for the sample with nominal composition $LaPt_4Ge_{12}$

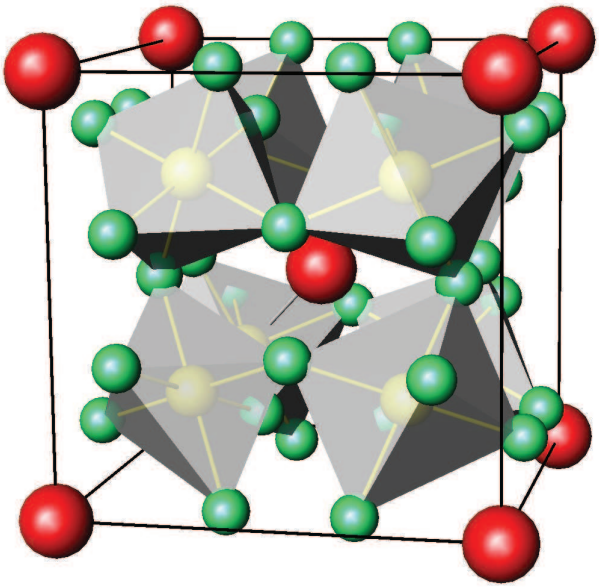

Figure 4.4.: Unit cell the sample with nominal composition $LaPt_4Ge_7Sb_5$

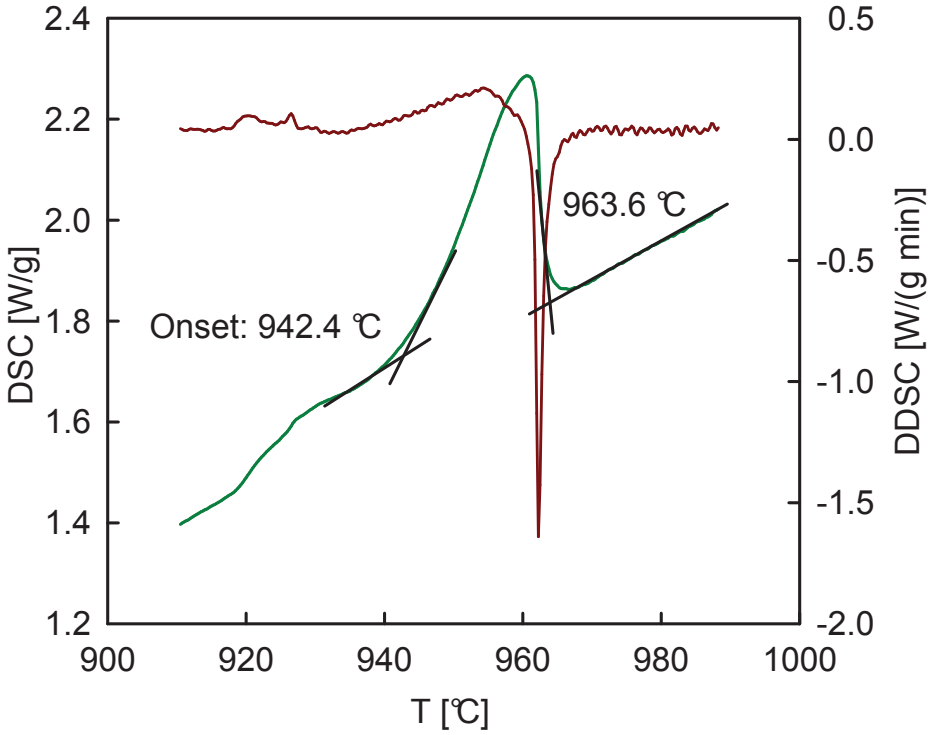

Figure 4.5.: DSC measurement for the sample with nominal composition $LaPt_4Ge_7Sb_5$ to determine the melting point

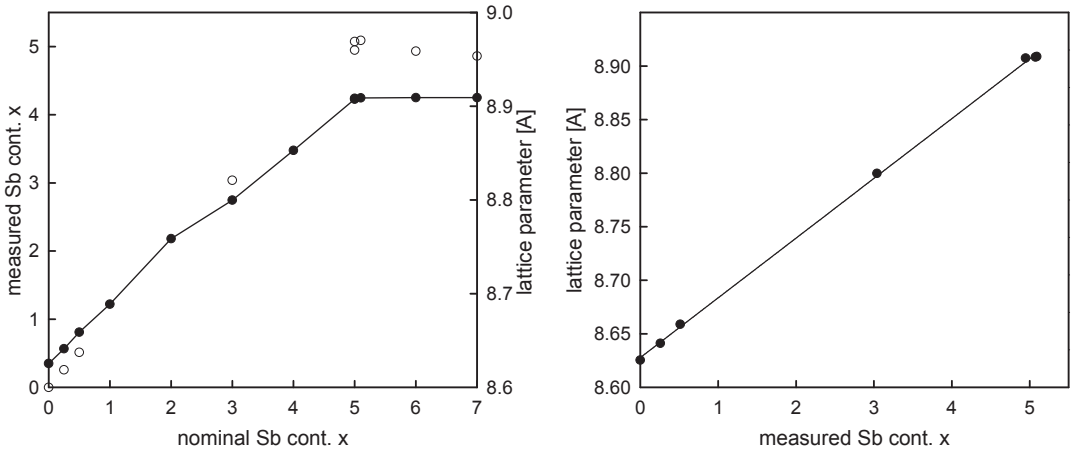

(a) end of solubility (b) lattice parameter vs. Sb content

Figure 4.6.: Solubility of Sb in the skutterudite $\mathrm{LaPt_4Ge_{12-x}Sb_x}$. The lattice parameter increases with the amount of solved Sb.

4.1.2. Ball milled and hot pressed sample

One of the brittle samples (nom. comp. $\mathrm{LaPt_4Ge_8Sb_4}$) was prepared as ball milled and hot pressed sample. Fig. A.7(a) shows the sample in as cast condition, A.7(b) after ball milling and hot pressing. It is nanostructured and Fig. A.1(g) shows that it is dense and shiny. The density is: $8.4156\mathrm{g/cm^3}$ (gained from measure the volume of the cylinder and the weight), $8.6203\mathrm{g/cm^3}$ (gained by Archimedes principle in water - pores partly filled with water) and $9.4963\mathrm{g/cm^3}$ (calculated from the lattice parameter and molecular weight).

4.1.3. $\mathrm{BaPt_{(4-x)}Ir_xGe_{12}}$-system

In chapter 2.2 several reasons are discussed why it there could be advantages in thermoelectric properties when substituting Pt with Ir in the skutterudite $\mathrm{BaPt_4Ge_{12}}$ (formally $\mathrm{BaPt_{(4-x)}Ir_xGe_{12}}$). A series of 4 samples was prepared with nominal compositions $\mathrm{BaPt_{3,5}Ir_{0,5}Ge_{12}}$, $\mathrm{BaPt_3Ir_1Ge_{12}}$, $\mathrm{BaPt_{2,5}Ir_{1,5}Ge_{12}}$ and $\mathrm{BaPt_2Ir_2Ge_{12}}$. The samples were annealed for 10 days at 800°C and, as there was no solubility measured, later 10 days with 700°C. All samples were analyzed with powder x-ray diffraction and with EDX analysis in the electron microscope after arc melting and after every heat treatment. Fig. B.1 to B show pictures of these samples. In as cast condition as well as after both heat treatments there are more than one phase in the material. Table B.1 to B.4 include a

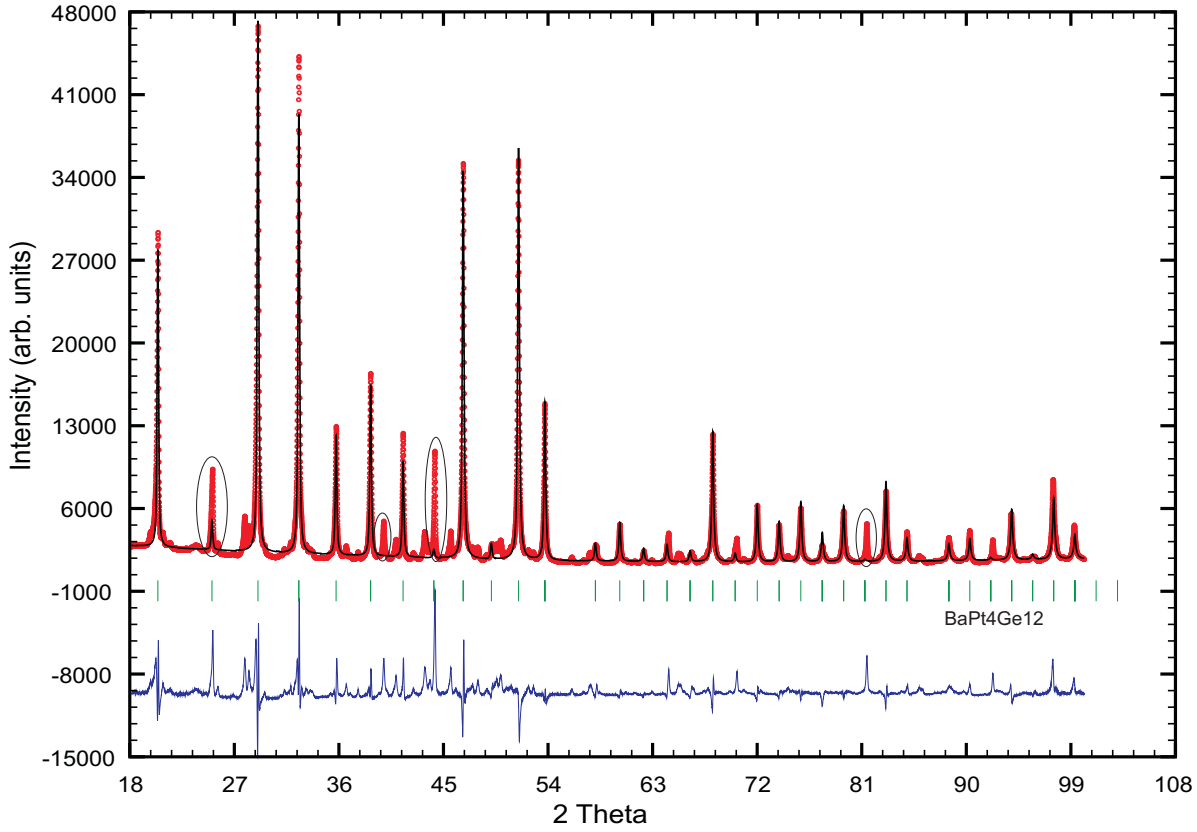

Figure 4.7.: Rietveld Refinement for the sample nom. comp. $BaPt_{3,5}Ir_{0,5}Ge_{12}$. Suggestion is that the other phase (marked peaks) are $BaIr_xPt_{2-x}Ge_7$ with a still unknown structure type

list of all identified phases and the calculated lattice parameters from X-ray data. The as cast samples comprise an eutectic system, containing $Ge/PtGe_2$, that vanishes after annealing. The big, white, long crystals have the chemical composition $BaIr_yPt_{(2-y)}Ge_7$ with an up to date undetermined crystal structure. Fig. 4.7 shows a Rietveld refinement for the sample with nominal composition $BaPt_{3,5}Ir_{0,5}Ge_{12}$. The main phase (matrix phase in Fig. B.1 to B) is the skutterudite $BaPt_4Ge_{12}$ with no significant Ir dissolved. The circled peaks in Fig. 4.7 do not fit to any of the phases with known crystal structure listed B.1 to B.4. So this peaks should be the result of the $BaIr_yPt_{(2-y)}Ge_7$ crystals. Within the series of samples the Ir amount was increased. This further Ir is found in the increasing amount of $IrGe_4$ and in the $BaIr_yPt_{2-y}Ge_7$ crystals, where the solved content of Ir increases with the added amount of Ir, see Fig. 4.8(a). The solved Ir in

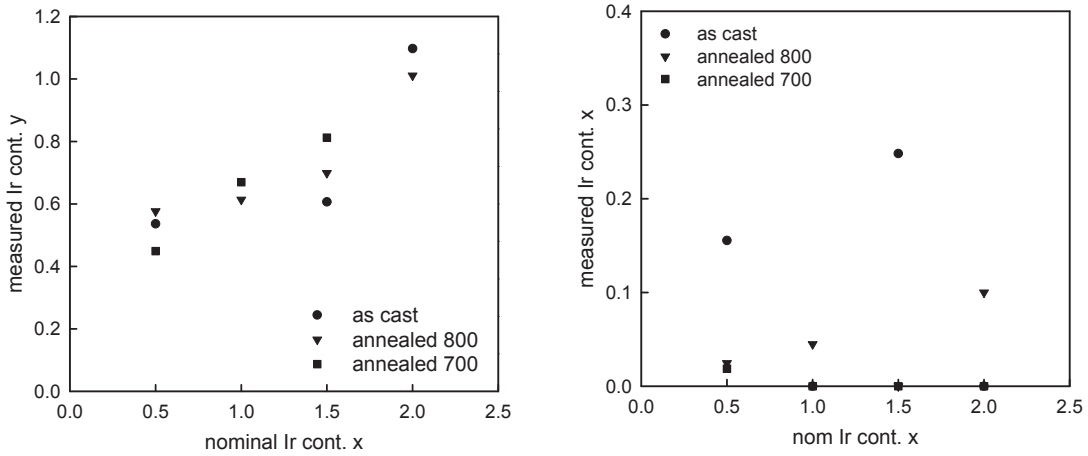

(a) $\mathrm{BaIr_yPt_{(2-y)}Ge_7}$ (b) $\mathrm{BaPt_{(4-x)}Ir_xGe_{12}}$

Figure 4.8.: Solubility of Ir in the two main phases.

the skutterudite is small, within measurement accuracy zero, for all different heat treatments see Fig. 4.8(b). Concluding, it can be noted that no measurable amount of Ir can be solved in this skutterudite, neither at 800° nor at 700°C. A new compound was found: $\mathrm{BaIr_yPt_{2-y}Ge_7}$, which does solve Ir. This compound will be subject to further investigations, in order to determine its crystal structure.

4.2. Heat capacity

The temperature dependent specific heat was measured for 6 samples with different amount of Sb. Fig. 4.9(a) shows the results of these measurements in a temperature range from 0-15 K. The samples with nominal composition $\mathrm{LaPt_4Ge_{12}}$, $\mathrm{LaPt_4Ge_{11.75}Sb_{0.25}}$ and $\mathrm{LaPt_4Ge_{11.5}Sb_{0.5}}$ exhibit a jump in $\mathrm{C_P(T)}$, indicating bulk superconductivity. Using Eqn. 2.55 and 2.63 the heat capacity can be accounted by $\frac{\mathrm{C_P}}{\mathrm{T}} = \gamma_\mathrm{N} + \beta_\mathrm{N}\mathrm{T}^2$ using just the normal state part. Table 4.3 shows the results of these fits, also in comparison to the reference taken from [17]. γ and β can be determined more accurately by suppressing superconductivity applying a magnetic field and using data only very close to zero for fitting. Furthermore, for the superconducting samples the area above and below the fit (S=$\int \frac{C_P}{T} dT$) should be equal, to get S = 0 at T = 0, fulfilling the 3^{rd} law of thermodynamics. So with this method one gets too low Sommerfeld values. Fig. 4.9(b) shows only the superconducting samples with an entropy balanced fit. For both kinds of fits, table 4.3 evidences the very clear tendency of the Sommerfeld parameter (that is proportional

Table 4.1.: $LaPt_4Ge_{12-x}Sb_x$ series with x= 0, 0.25, 0.5, 4, 5 , Sommerfeld parameter $\gamma = \frac{1}{3}\pi^2 D(\epsilon_F)k_B^2$, from the Debye approximation $\beta = \frac{12\pi^4}{5} n k_B \left(\frac{T}{\Theta_D}\right)^3$ and the Debye temperature $\Theta_D^{LT} = \sqrt[3]{\frac{1944n}{\beta}}$

Sb cont. x	γ [J/molK^2] [3]	β [J/molK^4] [3]	Θ_D^{LT}[K][3]	γ [J/molK^2][4]	β [J/molK^4][4]	Θ_D^{LT}[K][4]
0[1]	0.0531[2]	0.00378	206.1	0.0758	0.00346	212.2
0.25	0.0357	0.00347	212.2	0.0584	0.00327	216.1
0.5	0.0231	0.00315	219.0	0.0458	0.00275	229.1
4	0.0127	0.00146	282.9	-	-	-
5	0.0128	0.00146	282.9	-	-	-

[1] data copied from [17]
[2] compared to [17] smaller value (0.0758[J/molK^2]) because γ could be determined more accurate with a magnetic field suppressing superconductivity
[3] using normal state data for the fit
[4] entropy balanced fit

to the density of states at the Fermi level) decreasing with the amount of substituted Sb. As $\Theta_D \propto \sqrt{\frac{D}{m}}$ the increase of the Debye temperature with the increased amount of added Sb has to be explained by a stronger spring constant. Knowing the melting point (which we assume to be the same as for ($LaPt_4Ge_7Sb_5$ $944°C = 1217$ K) one can use the Lindemann rule $\Theta_D = \sqrt{\frac{T_m}{m}}\frac{1}{\sqrt[3]{V}}$ (from reference [34]) to estimate how the Debye temperature changes with the Sb content. Considering the volume (derived from X-Ray data, the mass and the melting point) the evolution of the Debye temperature is not explained.

4.2.1. Phonon density of states

The phonon part of the specific heat is given by Eqn. 2.57. The phonon density of states can now be considered with different models and parameters can be extracted for these models from the specific heat. Table 4.2 shows the parameters calculated with different models for the two different samples $LaPt_4Ge_{12-x}Sb_x$ with x= 0.5 and 5. Fig. 4.2.1 shows the two measurements, fitted with the Debye Einstein Model, using different numbers of Einstein functions. For the fitting process the „user defined functions“ in section C.1 were employed. In Fig. 4.10(a), it can be seen that the simple Debye model is by far not sufficient to describe the curve. Fig. 4.4 shows the unit cell of the skutterudites used. It consists of 34 atoms, so there are three acoustic branches and 99 optical branches. Using the Debye model only the acoustic branches are considered. Using Einstein modes

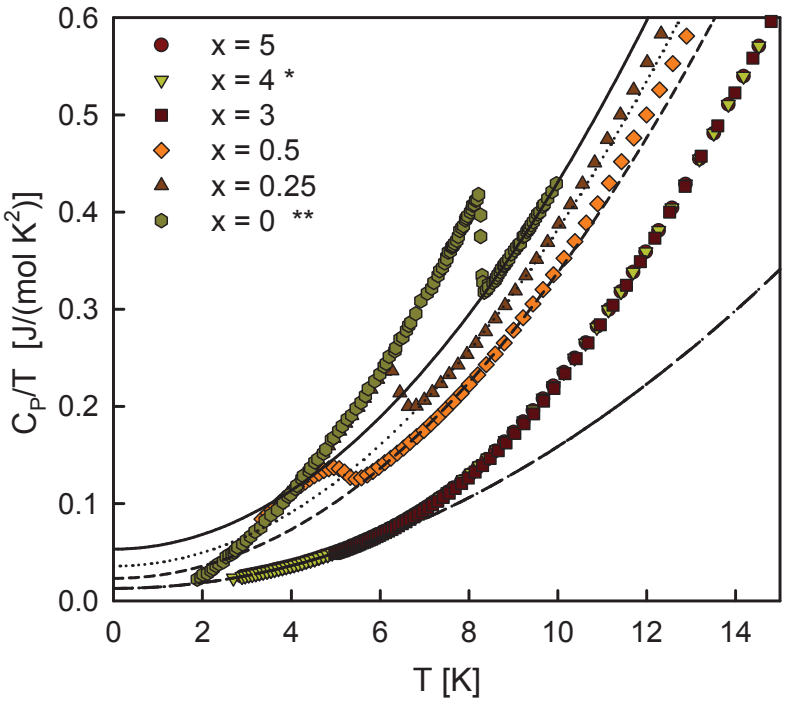

(a) C_P measurements, using normal state data for fit

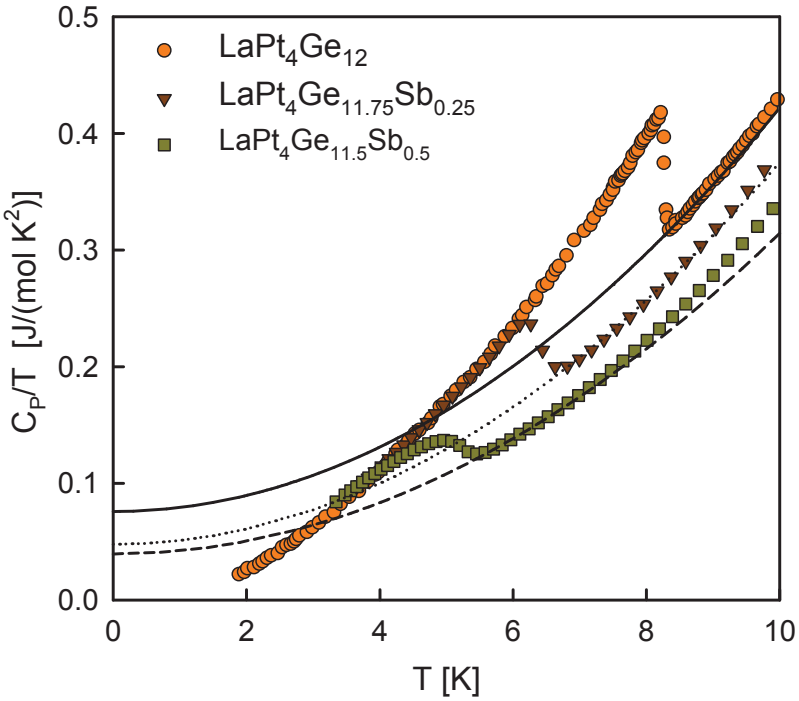

(b) superconducting samples, entropy balanced fit

Figure 4.9.: $LaPt_4Ge_{12-x}Sb_x$ series with x= 0, 0.25, 0.5, 3, 4, 5 values. Values for x = 0 taken from reference [17]. $\frac{C_P}{T} = \gamma_N + \beta_N T^2$ fit for low temperatures

Table 4.2.: $LaPt_4Ge_{12-x}Sb_x$ series with x= 0.5, 5 values of Θ_D fitting the data from 3 to 100 K with a simple Debye model considering also different amounts of different Einstein modes. Fitting models used, see appendix C.1

model	Sb cont. x	Θ_D	p	Θ_{E1}	Θ_{E2}	Θ_{E3}	p1	p2	p3
Debye	0.5	266.1	1						
Einst1. Debye		74.2	25	220.2					
Einst2. Debye		112.6	19	289.9	143.1		10	6	
Einst3. Debye		104.4	29	281.1	159.3	115.7	16	3	6
Debye	5	280.7	1						
Einst1. Debye		77.3	28	222.1					
Einst2. Debye		129.5	16	275.7	140.9		9	4	
Einst3. Debye		134.8	27	274.2	174.0	111.6	17	2	6

to describe the optical modes, the Debye temperature decreases roughly by a factor $\sqrt[3]{p}$, with $3*p$ the number of branches; compare to reference [6]. In table 4.2 it is notable that the Debye Einstein model results in 3 Einstein modes with a weight of 17:3:6 which is somehow comparable to the weight of the amount of the different atoms in the reference skutterudite $LaPt_4Ge_{12}$ Ge:La:Pt = 12:1:4. Assuming that the first Einstein mode comes from the Ge atoms, the second from the lanthanum atoms and the third one from the platinum atoms, the Einstein frequencies should be higher for the light atoms and lower for the heavy atoms. The molar masses of Ge, La and Pt are 73, 139 and 195 where the Einstein frequencies are: 281, 159 and 116 for the first sample (with lower Sb content (x=0.5)) and 274, 174 and 112 for the second sample (x=5). So the success of this considerations is by, making an assumption that all the branches coming from atoms with the same weight have similar frequencies one can determine which Einstein mode is connected to which atom. For these assumptions the reference composition was used, including the true composition of the samples is $LaPt_4Ge_{12-x}Sb_x$ with x= 0.5, 5. The Einstein frequency of the Ge atoms is for the first sample 281 and for the second 274 which might be due to the further substituted heavier Sb atoms. Looking at table 4.2 one can observe the averaged Einstein modes splitting up more and more, which can be done theoretical until 99 different modes. The second Einstein mode, that is assumed to come from the lanthanum atoms is assumed to rattle in the cage. The cage size is increasing with the amount of antimony atoms, see Fig. 4.6(b). This is considered to cause a lower binding and higher frequency, and therefore higher energy absorption, of the rattling lanthanum atoms. The Einstein frequency of the lanthanum atoms (Θ_{E2}) is bigger for a higher amount of antimony, see table 4.2.

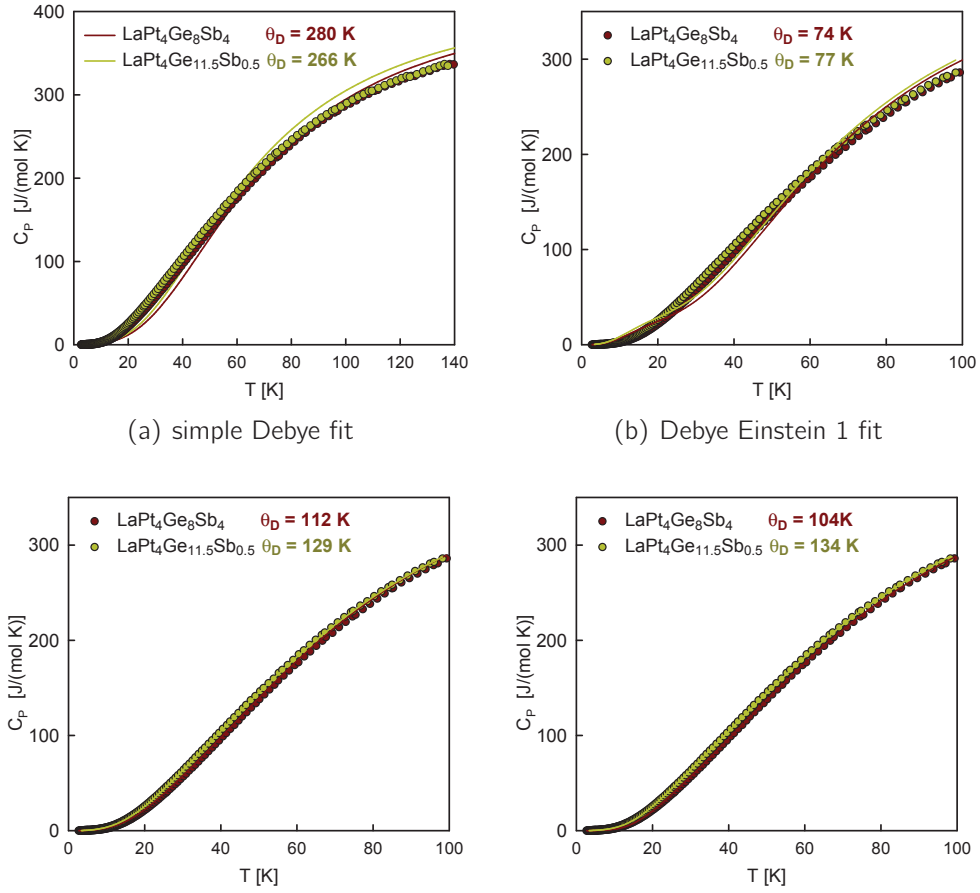

(a) simple Debye fit

(b) Debye Einstein 1 fit

(c) Debye Einstein 2 fit

(d) Debye Einstein 3 fit

Figure 4.10.: Debye Einstein model fit of the two samples $LaPt_4Ge_{12-x}Sb_x$ with x= 0.5, 5, using 0, 1, 2 and 3 different Einstein frequencies. Fitting models used, see appendix C.1

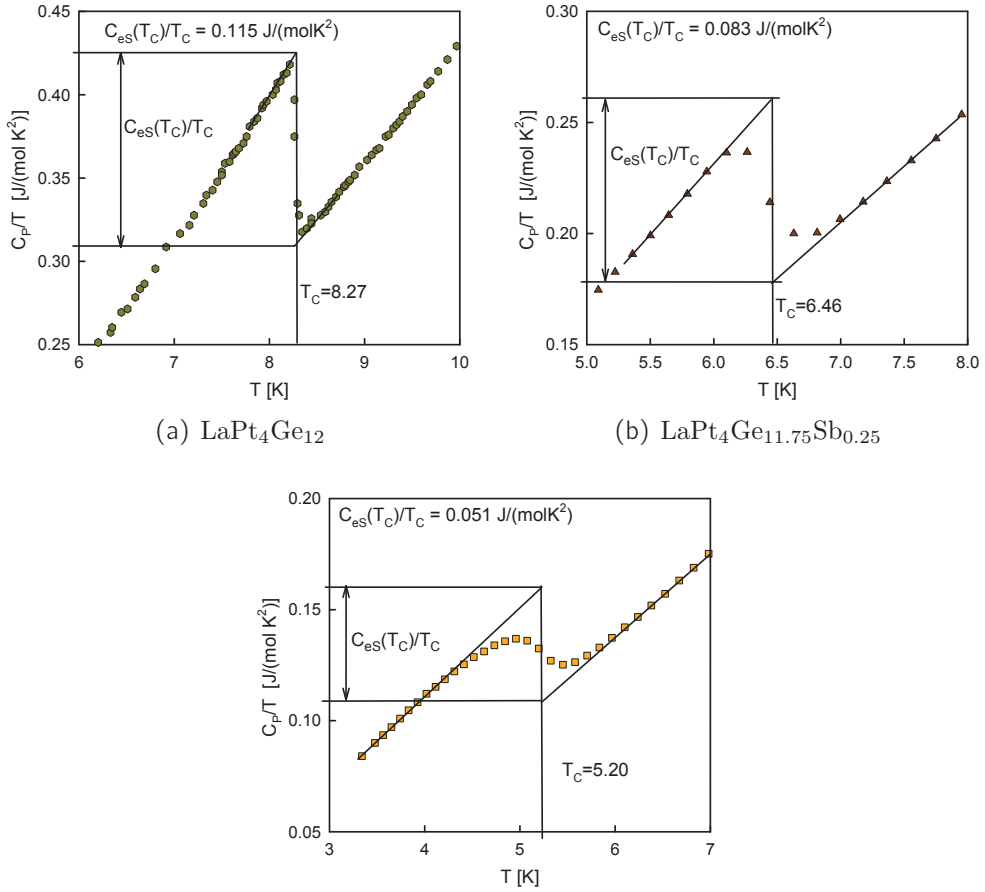

(a) $LaPt_4Ge_{12}$ (b) $LaPt_4Ge_{11.75}Sb_{0.25}$

(c) $LaPt_4Ge_{11.5}Sb_{0.5}$

Figure 4.11.: determination of T_C and $\frac{\Delta C_P}{T_C}$ out of the heat capacity measurements

4.2.2. Superconductivity

In Fig. 4.9(a) it can be seen, that three of the measured samples are superconducting at low temperatures, Fig. 4.9(b) also illustrates an entropy balanced fit for these superconducting samples, gaining γ (electronic contribution at low temperatures) and β (phonon contribution at low temperatures), listed in 4.3. The superconducting jump gets less sharp with increasing antimony amount because of the increased structural disorder from the substituted atoms. T_C decreases rapidly, according to BCS theory, due to a lower density of states at the Fermi level. BCS theory predicts a relative jump of the specific heat at T_C of 1.43, see Eqn. 2.7. Table 4.3 contains the values of T_C and $\frac{\Delta C_P}{\gamma T_C}$ with $\gamma T_C \approx C_N$ which were gained from Fig. 4.2.2; these are close to the BCS theory value of 1.43 and get smaller with increasing antimony amount, which would indicate a weaker coupling of the Cooper pairs. Now again using BCS theory to gain the energy gap Δ_0

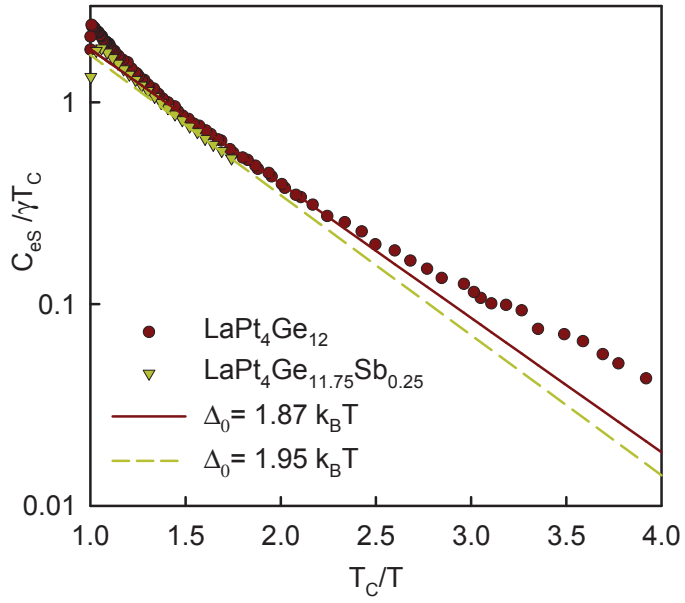

Figure 4.12.: Δ_0/k_BT_C determined by fitting Eqn. 2.6 for the samples with nominal composition $\mathrm{LaPt_4Ge_{12}}$ (C_P/T data taken from [17]) and $\mathrm{LaPt_4Ge_{11.75}Sb_{0.25}}$. $\mathrm{C_{eS}}$ gained by subtracting the phonon part

and $\Delta_0/\mathrm{k_BT_C}$, see Eqn. 2.6. $\Delta_0/\mathrm{k_BT_C}$ BCS theory is 1.76. Fig. 4.12 shows a fit of Eqn. 2.6 and results in values slightly higher than BCS theory predicts, see table 4.3. The electronic specific heat is gained by subtracting the phonon specific heat (defined by β in table 4.3). This higher values would indicate a higher coupling which is in contrast to the values of $\frac{\Delta \mathrm{C_P}}{\gamma \mathrm{T_C}}$. The energy gap, established by the Cooper pairs, is decreasing from the reference sample $\mathrm{LaPt_4Ge_{12}}$ with 1.33 meV (15.5 K) to 1.08 meV (12.6 K) for the sample $\mathrm{LaPt_4Ge_{11.75}Sb_{0.25}}$. Eqn. 2.3 shows the exponential connection between this energy gap and the electronic density of states at the Fermi level ($N(E_F)$). Using this equation a smaller gap means a smaller $\mathrm{N(E_F)}$, so $\mathrm{N(E_F)}$ decreases with increasing Sb content.

4.3. Magnetic properties

Figure 4.13 illustrates the temperature dependent magnetic low field (100 G) susceptibility of the three superconducting samples. $\mathrm{T_c}$ is, as already measured in section 4.2.2, strongly decreasing with increasing amount of antimony. The onsets for the three samples are, as shown in Fig. 4.3, are 7.9 K, 6.8 K and 4.8 K determined with the

Table 4.3.: $LaPt_4Ge_{12-x}Sb_x$ series with x= 0, 0.25, 0.5 are superconducting; values of T_c, Sommerfeld parameter $\gamma = \frac{1}{3}\pi^2 D(\epsilon_F)k_B^2$, $\frac{\Delta C_P}{T_C}$and $\frac{\Delta C_P}{\gamma T_C}$ determined from Fig. 4.2.2, $\Delta_0/k_B T_C$ and Δ_0 determined using BCS theory $\frac{C_{eS}}{\gamma T_C} = 8.5 exp(-\frac{0.82\Delta_0}{k_B T})$

Sb cont. x	T_c [K]	$\frac{\Delta C_P}{T_C}$	γ	$\frac{\Delta C_P}{\gamma T_C}$	$\Delta_0/k_B T_C$	Δ_0 [meV]
0[1]	8.27	0.115	0.0758	1.52	1.87	1.33
0.25	6.46	0.083	0.0584	1.42	1.95	1.08
0.5	5.20	0.051	0.0458	1.11	-	-

[1] data copied from [17]

lowest field of the zero field cooling measurements. With increasing fields the Meissner state is reached at lower temperatures; for the sample $LaPt_4Ge_{11.5}Sb_{0.5}$ its outside the measured temperature range. In theory the susceptibility of the in the Meissner state is -1. Looking at figure 4.13 the reference sample $LaPt_4Ge_{12}$ is reaching the Meissner state within the measured temperature range (χ is not increasing any more). As it is measured as a mass susceptibility in CGS units it has to be multiplied by 4π and by the density. For this sample only the density calculated out of the lattice parameter and the composition of the compound is available and gives a value of 9.3 g/cm^3. Furthermore a demagnetization factor has to be considered; considering the demagnetization factor of a sphere ($H_i = \frac{3}{2}H_a$) the susceptibility at 2.7 K of the reference sample $LaPt_4Ge_{12}$ in zero field cooling, low field measurement is -1.0. So the rough assumptions, made especially for sample shape and density, seem not too bad. The susceptibilities, gained from field cooling measurements, also called Meissner flux expulsion measurement, are (below T_C) a factor 10 lower, than the ZFC measurement. This big difference is known to be caused by strong pinning effects. This result, as well as the time dependent susceptibilities are very similar to the results of Gumeniuk et. al. [17]. Figure 4.15 presents the dependence of the magnetization on the applied field at 3 K. Inside the Meissner state this dependence is linear. At higher magnetic fields the linear behavior changes into a nonlinear one. The value of the magnetic field where this nonlinear behavior starts, which means that there is not any longer full flux expulsion, but magnetic field starts to enter the sample, is called H_{c1} and is at about 160, 100 and 50 G (Oe) for $LaPt_4Ge_{12}$, $LaPt_4Ge_{11.75}Sb_{0.25}$ and $LaPt_4Ge_{11.5}Sb_{0.5}$.

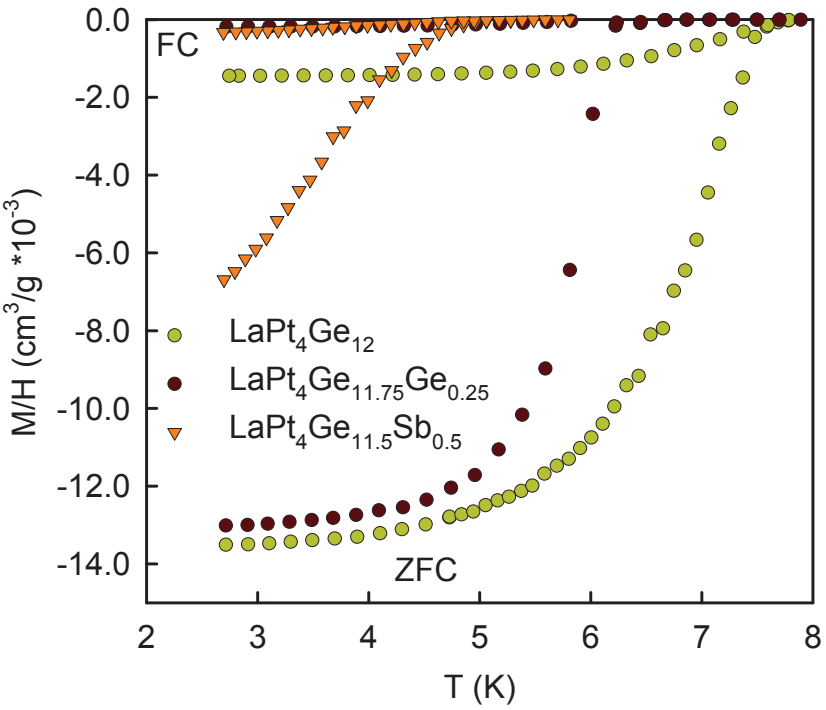

Figure 4.13.: Temperature dependent magnetic susceptibility for the three superconducting samples $LaPt_4Ge_{12}$, $LaPt_4Ge_{11.75}Sb_{0.25}$ and $LaPt_4Ge_{11.5}Sb_{0.5}$ in CGS units for zero field cooling and field cooling, measured with a field of 100 G.

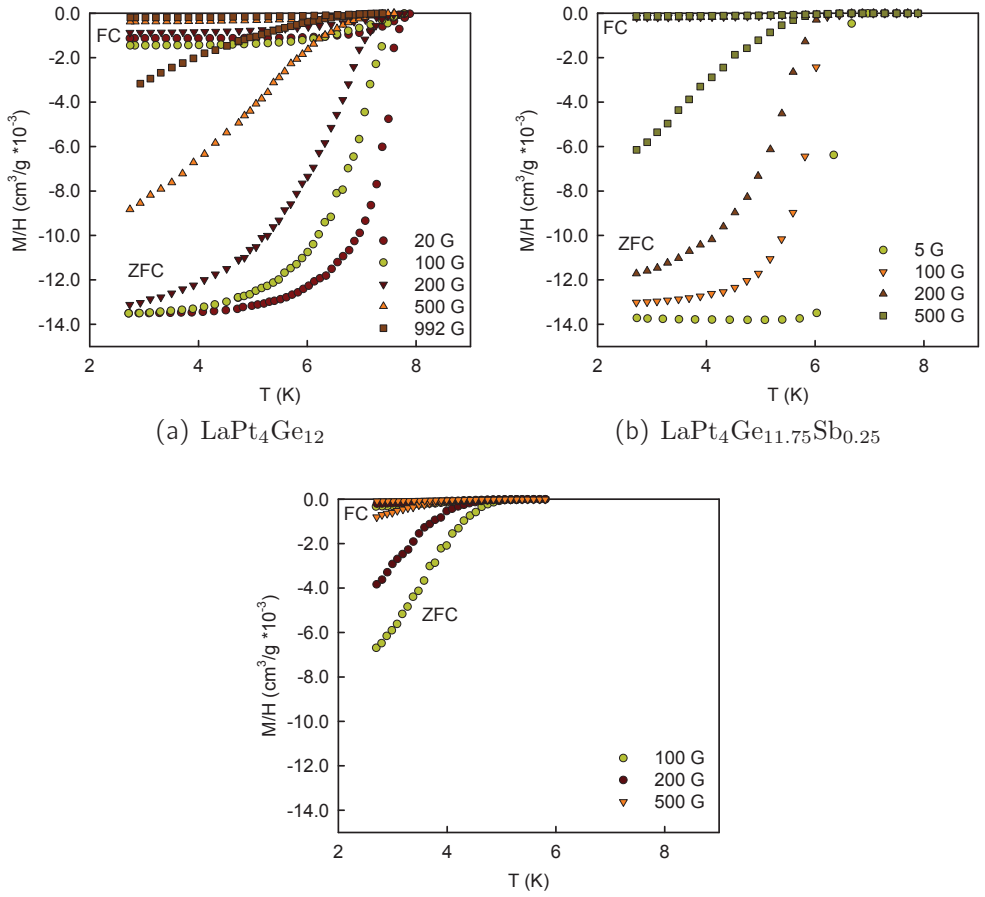

(a) $LaPt_4Ge_{12}$ (b) $LaPt_4Ge_{11.75}Sb_{0.25}$

(c) $LaPt_4Ge_{11.5}Sb_{0.5}$

Figure 4.14.: temperature dependent magnetic susceptibility for the three superconducting samples $LaPt_4Ge_{12}$, $LaPt_4Ge_{11.75}Sb_{0.25}$ and $LaPt_4Ge_{11.5}Sb_{0.5}$ for zero field cooling and field cooling measured with different fields.

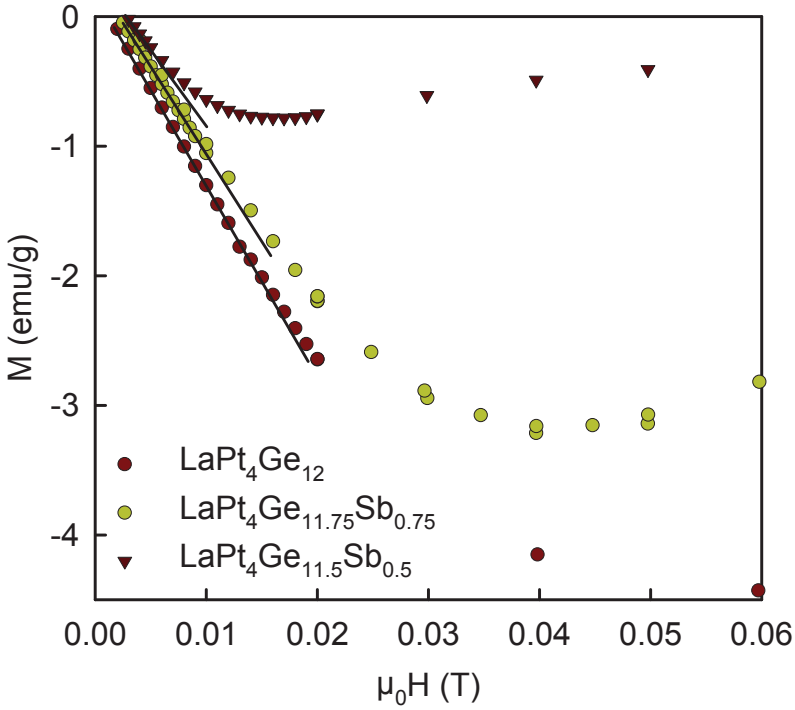

Figure 4.15.: Magnetization in dependence of the applied field at 3K

4.4. Thermal expansion

The temperature dependent thermal expansion was measured using the hot pressed sample (which was the only sample being dense and compact enough) with the nominal composition $\mathrm{LaPt_4Ge_8Sb_4}$. Fig. 4.4 shows the thermal expansion coefficient (4.16(b)) and the change in length per unit of the original length. The data above 250 K are assumed to have some error in the measurement because the thermal expansion coefficient is supposed to increase. Using the data until 200 K three fits are made, using a Debye and a Debye Einstein model for the internal energy in Eqn. 2.69 (Fig. 4.16(a)). The Debye Temperature observed is in fair agreement to the values gained above from heat capacity measurements (280 K). As there is a quadratic and a cubic term in Eqn. 2.69 the dependence of the Debye/Einstein temperatures is quite hidden; thus it is possible to observe even quite different results.

4.4.1. Grüneisen- parameter

Fig. 4.17 shows the temperature dependent Grüneisen parameter, gained by dividing the thermal expansion coefficient α by $\mathrm{C_P}$ and multiplying by the bulk modulus B, see Eqn.

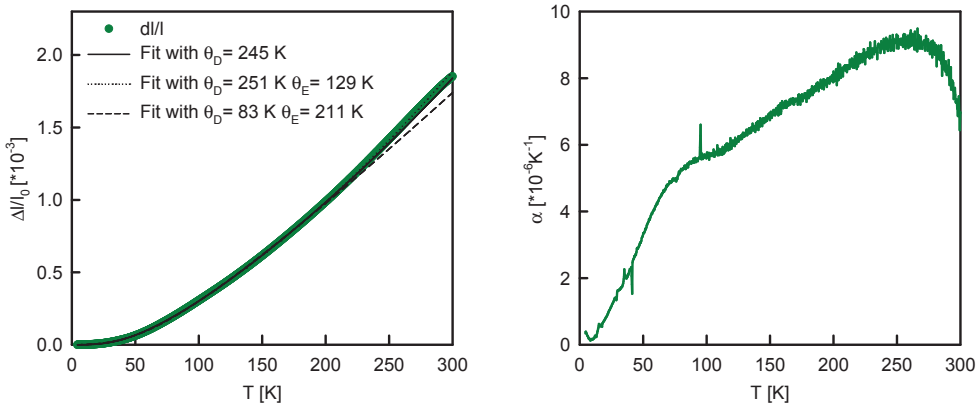

(a) relative change in length (b) thermal expansion coefficient α

Figure 4.16.: thermal expansion coefficient α and thermal expansion $\frac{\Delta l}{l_0}$ with a fit after Mukherjee [31] using different models for the internal energy

2.77. The bulk modulus is supposed to be a constant value of the order of $100\mathrm{GPa}$, which is a common assumption for metallic samples. Γ is around 2 and strongly increasing near zero. This happens because (see 4.17 inset) α increases close to zero, while $\mathrm{C_P}$ keeps on decreasing. The increasing values of α close to zero are assumed being measurement errors because α is supposed to end up with zero at zero K.

4.5. Thermoelectric properties

4.5.1. Resistivity

With most of the samples a resistivity measurement could be done, although some of the samples were quite brittle and contained holes, see appendix A. In order to measure the specific electrical resistance the cross section to length ratio has to be determined and multiplied with the measured resistance. This ratio can of course strongly be influenced by the bubbles, holes and cracks. Considering that these do not change during the measurement this influence is some constant value. An indicator for the quality of a sample is the residual resistance ratio (the ratio between the resistivity at room temperature and the resistivity just above the transition temperature $\rho_{300\mathrm{K}}/\rho_0$, see table 4.4). Compared to Schnelle [17] where ρ_0 is 6 $\mu\Omega\mathrm{cm}$ and RRR is 33 for $\mathrm{LaPt_4Ge_{12}}$ the present sample quality has to be assumed to be worse. Fig. 4.18 shows the temperature dependent resistance of all samples measured from 4 to 800 K. Fig. 4.19 presents in more detail the superconducting jump in resistivity. Table 4.4 contains the $\mathrm{T_C}$ values, measured at half

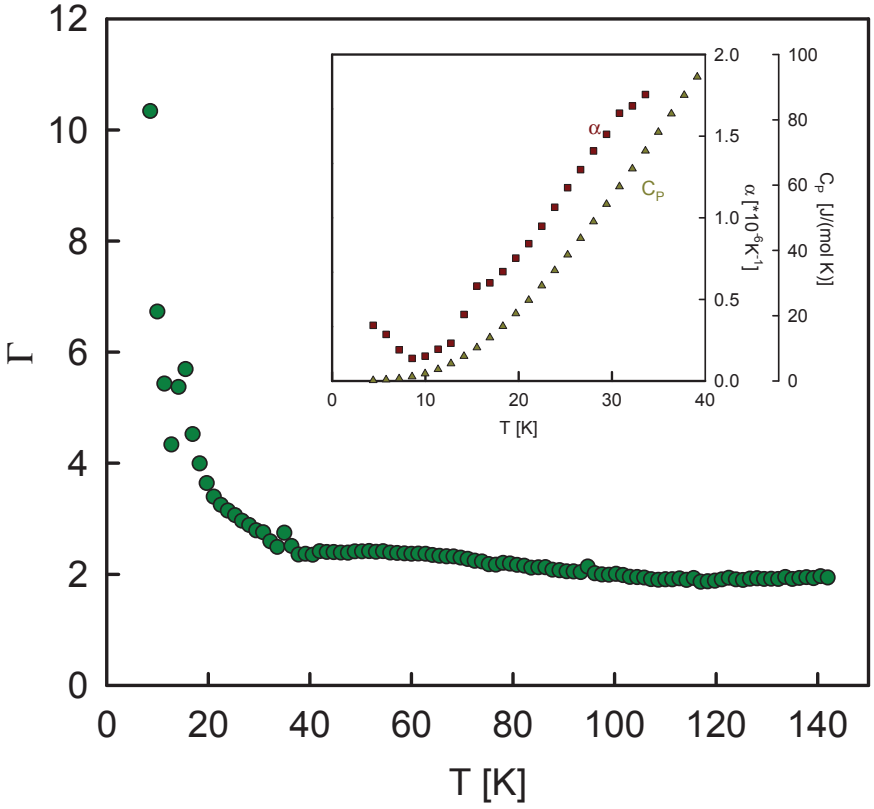

Figure 4.17.: Grüneisen-Parameter of the sample with nominal composition $LaPt_4Ge_8Sb_4$, ball milled and hot pressed

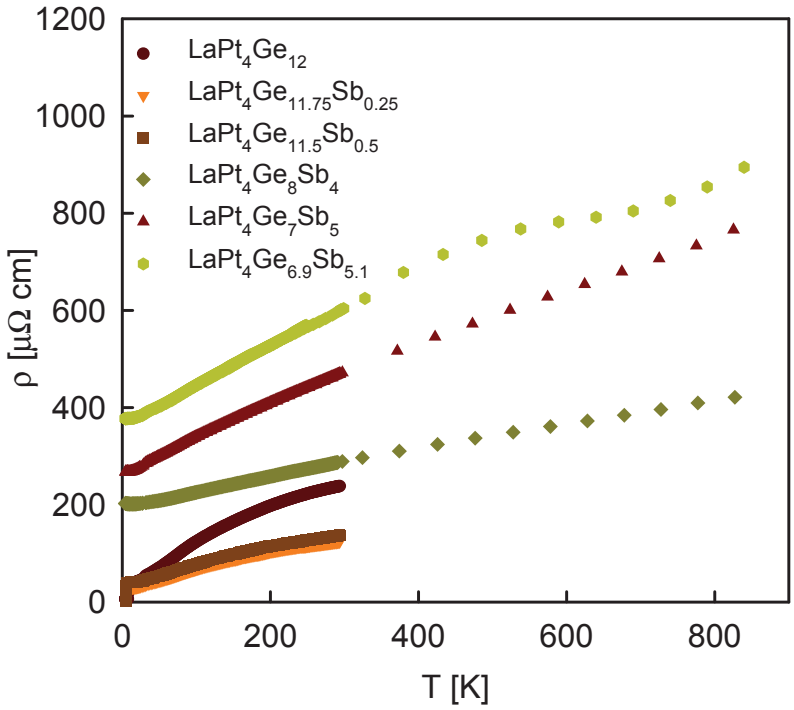

Figure 4.18.: temperature dependent resistivity measurement from 4 to 800 K; samples series $LaPt_4Ge_{12-x}Sb_x$ with x= 0, 0.25, 0.5, 4, 5, 5.1

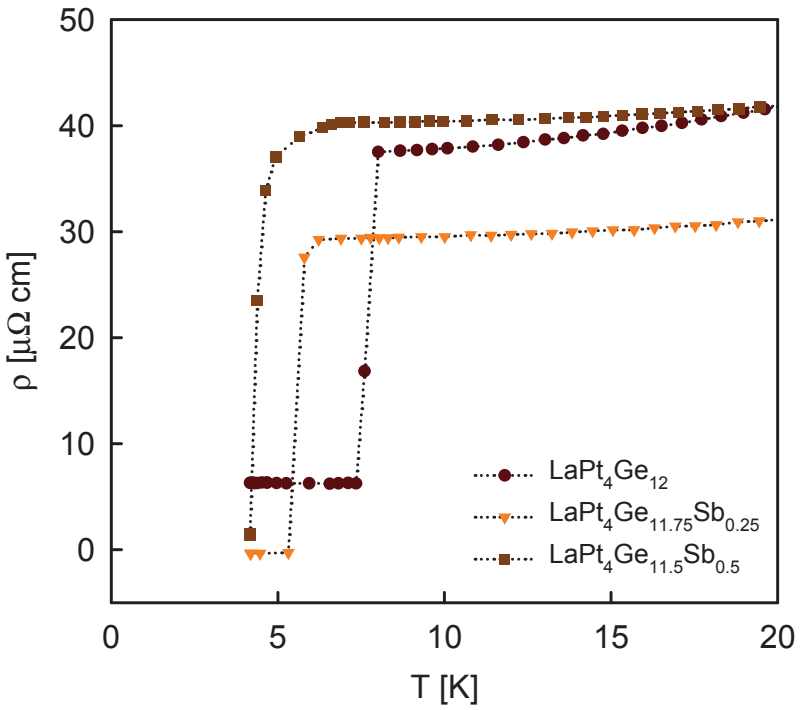

Figure 4.19.: temperature dependent resistivity measurement of the superconducting samples $LaPt_4Ge_{12-x}Sb_x$ with x= 0, 0.25, 0.5

height of the jump. The resistivity for the reference sample in the superconducting state is very high. As already observed from heat capacity measurement (see Fig. 4.9(b)) the transition to superconductivity is getting less sharp with increasing amount of antimony due to structural disorder. The measurement of the reference sample $LaPt_4Ge_{12}$ in Fig. 4.9(b) is shifted because of an error of the measuring bridge.

Bad metals/semiconductors - two band model

Fig. 2.5 shows the density of states of $LaPt_4Ge_{12}$ and $LaPt_4Ge_7Sb_5$, the starting and endpoint of the sample series. It can be seen that with further substitution of Sb the Fermi energy moves towards the band gap, because of the extra electron provided by antimony. So $LaPt_4Ge_{12}$ is expected to be metallic and $LaPt_4Ge_7Sb_5$ to be a semiconductor. As obvious in Fig. 4.18 $LaPt_4Ge_7Sb_5$ shows still a metallic behavior, but the resistivity increases significantly and at high temperature the slope of the temperature dependent resistivity is not linear any more (as expected for a metal with the Bloch-Grüneisen law, see Eqn. 2.36). Fig. 4.20 shows the deviation from a simple metallic behavior. It can be observed, that the higher the Sb content, the stronger the curvature of the

Table 4.4.: $LaPt_4Ge_{12-x}Sb_x$ series with x= 0, 0.25, 0.5, 4, 5, 5.1; resistance values just above T_C, at room temperature and the ratio ρ_{300}/ρ_0; critical temperature T_C

Sb cont. x	ρ_0 [$\mu\Omega$cm]	ρ_{300} [$\mu\Omega$cm]	ρ_{300}/ρ_0	T_C
0	37.7	238.5	6	7.7
0.25	29.4	124.4	4	5.6
0.5	39.8	137.4	4	4.3
4	202.3	287.3	1	-
5	267.8	470.0	2	-
5.1	377.5	598.0	2	-

temperature dependent resistivity. The two band model tries to employ the influence of the semi- conducting behavior by scaling the temperature dependent resistivity with the temperature dependent number of free charge carriers (compare to reference [34]). The number of electrons / holes is defined by

$$n_n(T) = \int_{E_F}^{\infty} N(E) f(E,T) dE \tag{4.1}$$

$$n_p(T) = \int_{-\infty}^{E_F} N(E)(1 - f(E,T)) dE \tag{4.2}$$

Fig. 4.21, taken from [21], shows a simplified density of states (using a two band model) of a poor metallic p-type conductor. According to Fig. 4.21 N(E) is defined as (compare to reference [23]):

$$N(E) = \begin{cases} N & E < 0 \\ N & 0 < E < E_1 \\ 0 & E_1 < E < E_2 \\ N & E > E_2 \end{cases} \tag{4.3}$$

$f(E,T)$ is the Fermi-Dirac distribution:

$$f(E,T) = \frac{1}{1 + \exp \frac{E - E_F}{k_B T}} \tag{4.4}$$

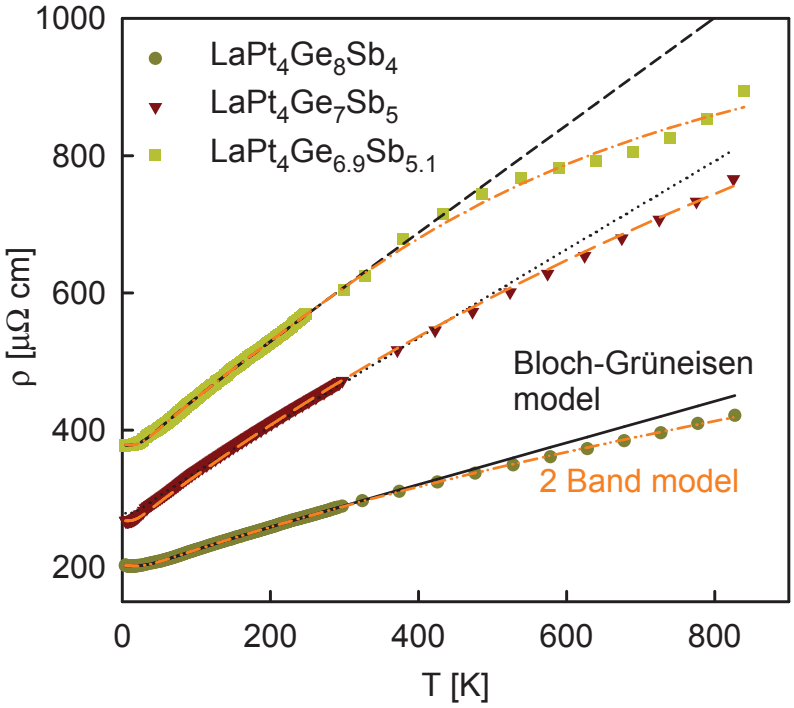

Figure 4.20.: temperature dependent resistivity measurement of the samples $LaPt_4Ge_{12-x}Sb_x$ with x= 4, 5, 5.1, fitted with the Bloch-Grüneisen model and the 2 Band Model

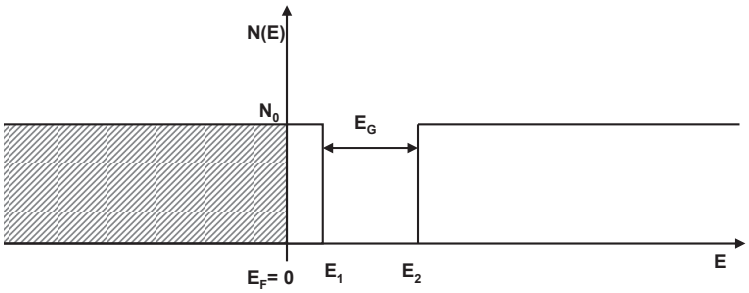

Figure 4.21.: DOS to describe near metal to insulator transition. E_1 and E_g are the main parameters

Table 4.5.: $LaPt_4Ge_{12-x}Sb_x$ series with x= 4, 5, 5.1; results of the two-band-fit

Sb cont. x	ρ_0 [$\mu\Omega$cm]	R[$\mu\Omega$cm/K]	Θ_D [K]	E_1 [K]	E_g [K]	k_BN [K^{-1}]	n_0
5.1	378.9	117.2	151	$6 * 10^{-6}$	4528	0.003	0.7
5	267.9	84.2	118	0.02	1272	0.0005	1.0
4	202.7	66.0	197	102	806	0.001	3.0

The equations for the number of holes/electrons can be solved for this simple case ($E_2 = E_1 + E_g$); all energies in K:

$$n_n(T) = Nk_B \left[E_g - Tln \left(\frac{1}{2} \frac{e^{\frac{E_1}{T}} + 1}{e^{\frac{E_1+E_g}{T}} + 1} \right) \right] \tag{4.5}$$

$$n_p(T) = Nk_B ln(2) T \tag{4.6}$$

$$n(T) = \sqrt{n_n(T) n_p(T)} + n_0 \tag{4.7}$$

With this charge carrier density the resistivity can now be scaled. ρ_{ph} is the resistivity caused from electron-phonon interactions and described by the Bloch-Grüneisen equation, Eqn. 2.36.

$$\rho = \frac{n_0(\rho_0 + \rho_{ph})}{n(T)} \tag{4.8}$$

Table 4.5 shows the results of the two band fit. The energy gap E_g can be compared with the energy gap from the DOS calculations, see Fig. 2.5, which is about 0.5 eV or 6000K. This is in the same of order magnitude than the energy gaps fitted with the 2-band model. It has to be considered that, the farer away the energy gap from the Fermi level, the smaller is the influence of the energy gap size to the fit (because of the distribution function, that gets small above E_F very fast). The Fermi level is shifted with increasing Sb content more and more towards the energy gap edge, see E_1 in table 4.5. The Debye temperatures are of the same order of magnitude, but not in a very good consensus with the data gained from heat capacity measurements 4.3.

Metallic/superconducting samples - Woodard and Cody model

For the superconducting samples $LaPt_4Ge_{12-x}Sb_x$ with x= 0, 0.25, 0.5 neither the Bloch-Grüneisen nor the 2-Band model describes the temperature dependent resistivity in a satisfying way. The Woodard and Cody model is an empirical model that is used for

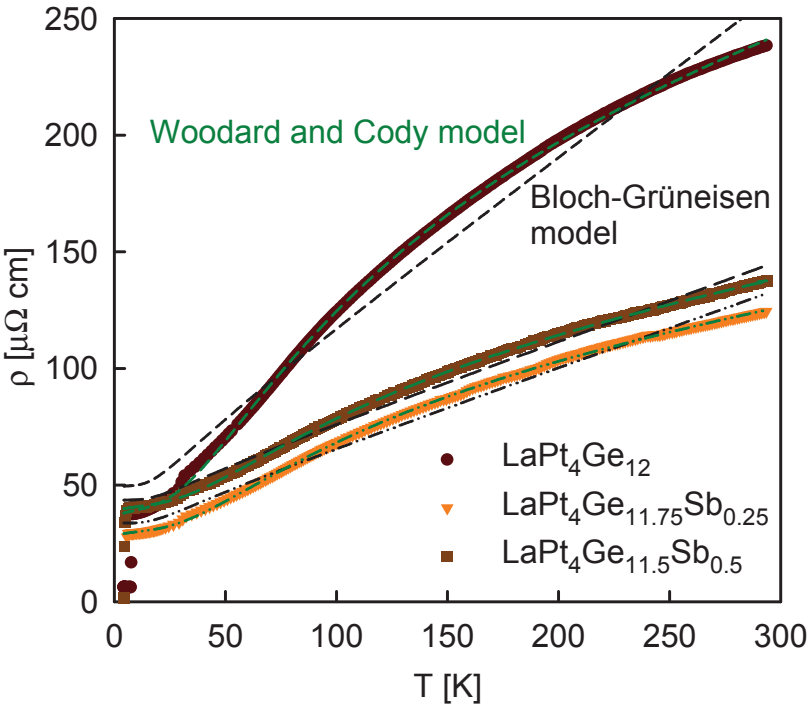

Figure 4.22.: temperature dependent electrical resistivity of the samples $LaPt_4Ge_{12-x}Sb_x$ with x= 0, 0.25, 0.5; Woodard and Cody fit

Table 4.6.: $LaPt_4Ge_{12-x}Sb_x$ series with x= 0, 0.25, 0.5; results of Woodard and Cody fit

Sb cont. x	ρ_0 [$\mu\Omega$cm]	ρ_1 [$\mu\Omega$cm/K]	ρ_2 [$\mu\Omega$cm]	T_0 [K]
0	37.1	0.22	204.3	114.1
0.25	28.7	0.12	90.7	120.4
0.5	39.4	0.13	91.0	125.5

many superconducting materials.

$$\rho = \rho_0 + \rho_1 T + \rho_2 exp(-T_0/T) \tag{4.9}$$

Woodard and Cody expects the anomalous resistivity to be caused by scattering, not by a changing number of charge carriers (from reference [37]). So there might be some connection between the electron phonon interaction that causes the formation of Cooper pairs at very low temperatures, and the electron phonon interaction that causes the strong curvature of the temperature dependent resistivity (from reference [6]). Fig. 4.22 shows the fits and table 4.6 a summary of the fitting parameters.

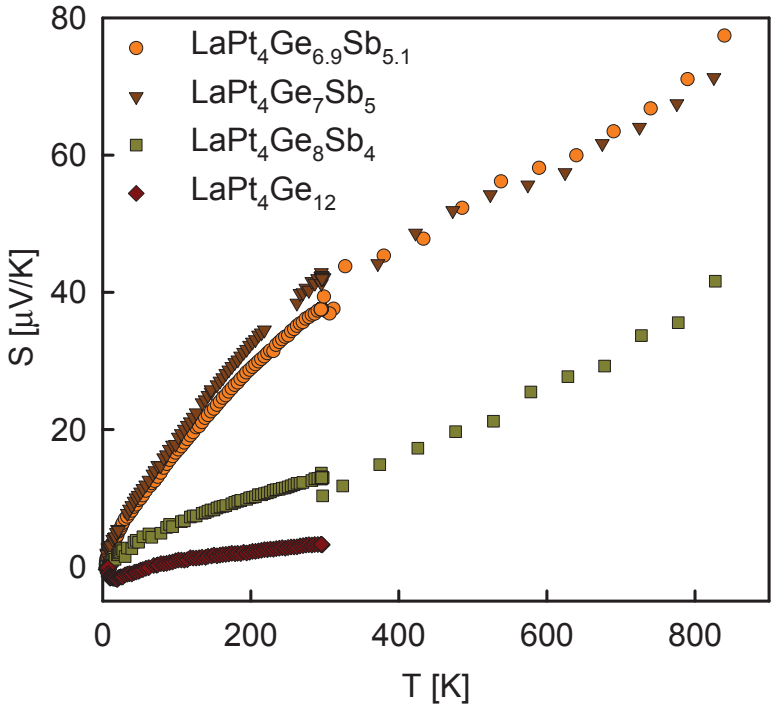

Figure 4.23.: Seebeck measurement

4.5.2. Seebeck coefficient

Fig. 4.23 shows results of the Seebeck measurements performed. The coefficients are positive, which assumes mainly hole conduction. As expected, S increases with the decreasing of free electrons at the Fermi level, see Eqn. 2.11. Eqn. 2.11 only considers free electrons. Electron phonon interactions can cause a so called phonon drag. This means that electrons a more likely scattered by phonons in the direction the electrons are already moving because of the temperature gradient. This might be the reason for the negative Seebeck coefficient at low temperatures of the reference sample with the nominal composition $\mathrm{LaPt_4Ge_{12}}$. Phonon drag occurs below 16 K.

4.5.3. Thermal conductivity and figure of merit

Thermal conductivity was measured for the $\mathrm{LaPt_4Ge_8Sb_4}$ ball milled and hot pressed sample. Fig. 4.24 shows the result of this measurement as well as for the fit, that consists of three parts: λ_{el}, calculated from the resistivity measurement by Wiedemann Franz law (see Eqn. 2.10), λ_{ph} modeled by the Callaway model 2.42 and the radiation losses T^3. The parameters of the Callaway fit (considering also radiation losses) are

Table 4.7.: Fit Parameters of the thermal conductivity with a Callaway fit, considering radiation losses, of the ball milled and hot pressed sample $LaPt_4Ge_8Sb_4$

#A0	scattering process parameter $[\frac{1}{K^4 s}]$	5991
#A1	Umklapp process parameter $[\frac{1}{K^3 s}]$	8.5
#A2	boundaries scattering parameter $[\frac{1}{s}]$	$4.1 * 10^{10}$
#A3	phonon- electron scattering parameter $[\frac{1}{Ks}]$	$1.4 * 10^{9}$
#A4	Debye Temperature Θ_D [K]	263
#A5	parameter for correction of radiation losses	$1.7 * 10^{-7}$

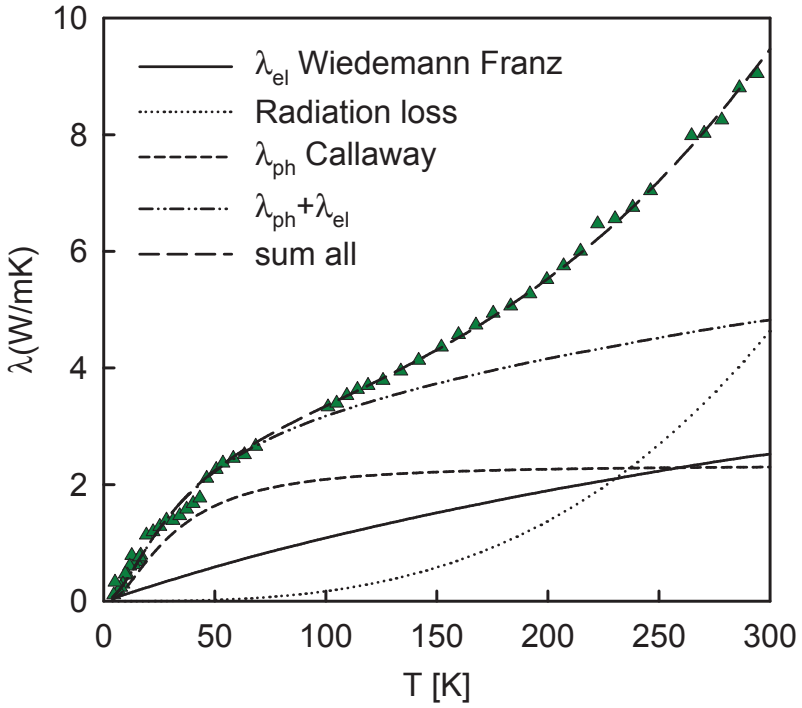

Figure 4.24.: thermal conductivity of the hot pressed sample with a nominal composition of $LaPt_4Ge_8Sb_4$. λ_{el} electronic part, calculated from the resistivity measurement, λ_{ph} fitted with the Callaway model, radiation losses.

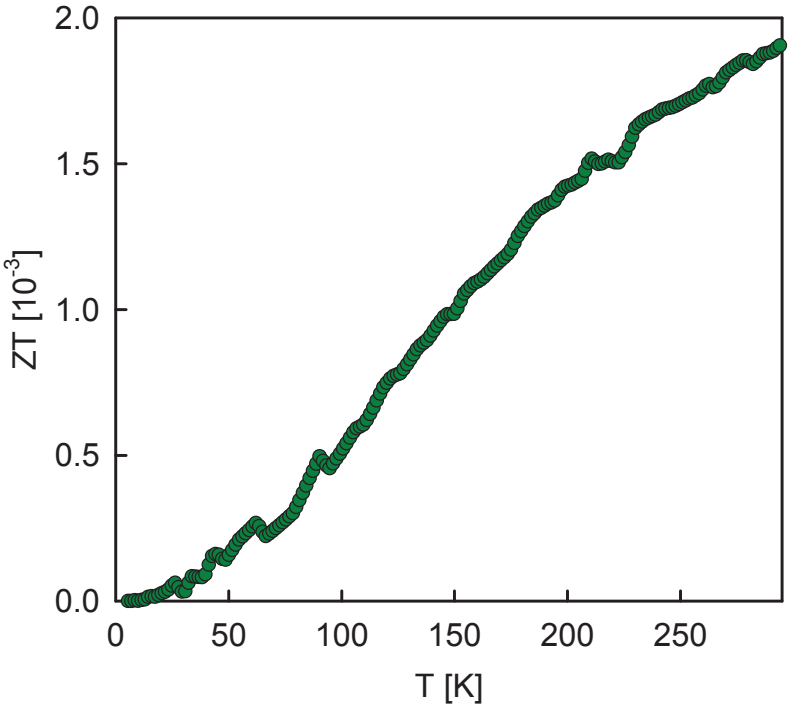

Figure 4.25.: ZT of the hot pressed sample with a nominal composition of $\mathrm{LaPt_4Ge_8Sb_4}$

summarized in table 4.7. The thermal conductivity is with around 10 W/mK at RT lower than for typical metals, like Silver with 430 W/mK at RT but still higher than with most good thermoelectric materials (1 W/mK).

The figure of merit (ZT) is calculated using electrical conductivity, thermal conductivity and Seebeck coefficient for the ball milled and hot pressed sample $\mathrm{LaPt_4Ge_8Sb_4}$ according to Eqn. 2.8. Fig. 4.25 shows the temperature dependent result. The ZT is $2 * 10^{-3}$ at 300K, which is quite small. ZT values of 1 are considered good. Still it has to be considered that this sample was not the one with the best expected thermoelectric properties, this would be the sample with the nominal composition $\mathrm{LaPt_4Ge_{6.9}Sb_{5.1}}$ at the end of the solubility of Sb.

4.6. Hall measurement

Figure 4.26 shows the charge carrier density calculated from a Hall measurement. The measurements have quite different qualities. $\mathrm{LaPt_4Ge_8Sb_4}$ has a higher charge carrier density than $\mathrm{LaPt_4Ge_7Sb_5}$ (at 300 K $9 * 10^{21}$ and $9 * 10^{20}$), for both holes are the main charge carriers. This is in accordance to the Seebeck measurements, see Fig. 4.23

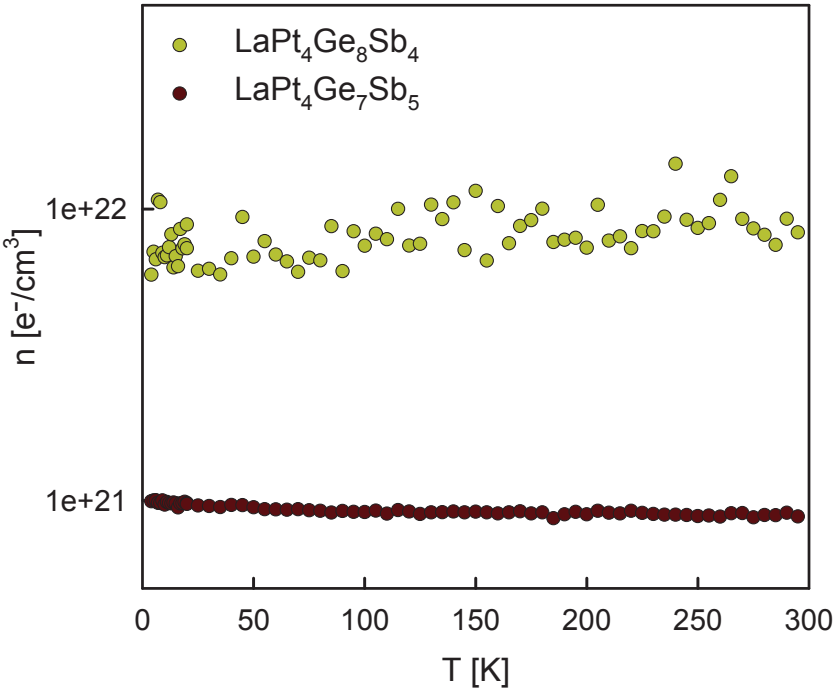

Figure 4.26.: charge carrier concentration calculated from Hall measurement for the samples hot pressed $\mathrm{LaPt_4Ge_8Sb_4}$ and $\mathrm{LaPt_4Ge_7Sb_5}$

assuming similar effective masses. Using Eqn. 2.11 the temperature dependent effective mass can be calculated using the data from Seebeck measurement Fig. 4.23 and charge carrier density Fig. 4.26. Fig 4.27 presents the result.

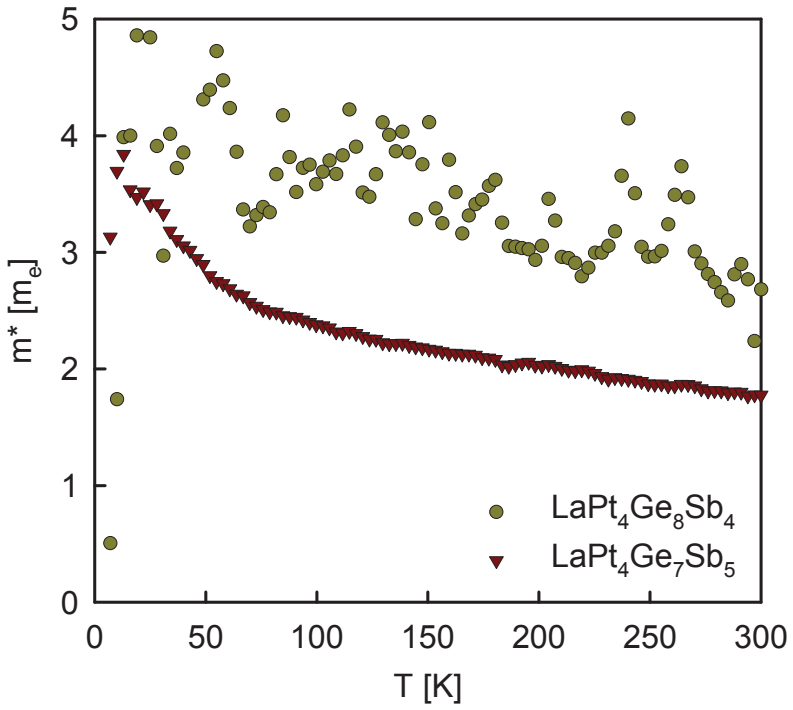

Figure 4.27.: effective mass, calculated from charge carrier concentration and Seebeck measurement for the samples: hot pressed $\mathrm{LaPt_4Ge_8Sb_4}$ and $\mathrm{LaPt_4Ge_7Sb_5}$

5. Conclusion

It was possible to produce a sample series of germanium based skutterudites with a composition of $\mathrm{LaPt_4Ge_{12-x}Sb_x}$. The solubility of antimony in the $\mathrm{LaPt_4Ge_{12}}$ compound terminates at $\mathrm{x} = 5 \pm 0.1$. The solubility could not be increased by using another annealing temperature. The melting point for $\mathrm{LaPt_4Ge_7Sb_5}$ is 942°C.

Previous assumptions concerning Zintl phase chemistry and density of states calculations announced p-type conducting samples. The Fermi level of $\mathrm{LaPt_4Ge_{12}}$ is below a energy gap of about 0.5 eV, see Fig. 2.5. Using antimony atoms instead of germanium atoms the additional electrons shift the Fermi level towards the energy gap. Temperature dependent resistivity measurements were fitted with the so called 2 band model which is a model for temperature dependent resistivity of materials with a Fermi level near a band gap. Fig. 4.20 and table 4.5 show the results of these fits which confirm the previous assumptions of the Fermi level moving towards the band gap with substituting antimony for germanium. The gap is not entirely reached because of the end of the solubility.

Seebeck effect increases from 3 $\mu\mathrm{V/K}$ for $\mathrm{x} = 0$ to 43 $\mu\mathrm{V/K}$ for $\mathrm{x} = 5$ at room temperature because of the decreasing charge carrier density (see Fig. 4.23). For charge carrier density gained from Hall measurement, see Fig. 4.26.

The reference sample $\mathrm{LaPt_4Ge_{12}}$ as well as the two samples with antimony content $\mathrm{x} = 0.25$ and $\mathrm{x} = 0.5$ are superconducting. All three superconducting samples match the BCS theory according to heat capacity measurements, see Fig. 4.12. The transition temperatures decrease strongly for increasing antimony content: $\mathrm{x} = 0, \mathrm{T_c} = 8.27$; $\mathrm{x} = 0.25, \mathrm{T_c} = 6.46$ and $\mathrm{x} = 0.5, \mathrm{T_c} = 5.20$. The superconducting samples are type II superconductors with a strong pinning effect, see susceptibility measurement Fig. 4.3.

For the hot pressed and ball milled sample with the nominal composition $\mathrm{LaPt_4Ge_8Sb_4}$ thermal conductivity could be measured and therefore a ZT value determined. The ZT value is less than $2 * 10^{-3}$ at room temperature which is quite low. Still one has to consider that this sample is not the optimal sample, considering charge carrier density and Seebeck effect.

Lattice properties were studied employing temperature dependent heat capacity and

thermal expansion measurement. Temperature dependent heat capacity as well as thermal expansion are described with models using the internal energy, which includes the phonon density of states. Combinations of Debye and Einstein models for the phonon density of states were used to describe the temperature dependent measurements, see Fig. 4.2.1.

A. Appendix - pictures -tables LaPtGeSb

Table A.1.: EDX and X-ray phase analysis data of the sample series $LaPt_4Ge_{12-x}Sb_x$

nom. composition	phase	lattice parameter	EDX (at%)			
			La	Pt	Ge	Sb
as cast						
$LaPt_4Ge_{12}$	$LaPt_4Ge_{12}$	8.6320	5.7	23.6	70.8	0.0
$LaPt_4Ge_{11}Sb$	$LaPt_4Ge_{11}Sb$	8.6996	6.2	22.1	63.3	8.45
$LaPt_4Ge_{10}Sb_2$	$LaPt_4Ge_{10}Sb_2$	8.7588	6.1	23.4	56.7	13.9
$LaPt_4Ge_9Sb_3$	$LaPt_4Ge_9Sb_3$	8.7988	6.0	23.7	52.7	17.7
$LaPt_4Ge_8Sb_4$	$LaPt_4Ge_8Sb_4$	8.8430	5.8	23.3	48.3	22.5
$LaPt_4Ge_7Sb_5$	$LaPt_4Ge_7Sb_5$	8.8943	5.6	23.3	42.9	28.2
$LaPt_4Ge_6Sb_6$	$LaPt_4Ge_7Sb_5$	8.8936	5.7	23.4	42.7	28.2
$LaPt_4Ge_5Sb_7$	$LaPt_4Ge_7Sb_5$	8.8982	5.9	23.2	42.7	28.2
$LaPt_4Ge_7Sb_5$	$LaPt_4Ge_7Sb_5$	8.9041	5.7	23.4	41.7	29.2
$LaPt_4Ge_7Sb_5$	$LaPt_4Ge_7Sb_5$	8.9007	5.6	23.4	42.5	28.6
$LaPt_4Ge_{11.75}Sb_{0.25}$	$LaPt_4Ge_{11.75}Sb_{0.25}$	8.6529	6.2	23.5	68.3	2.0
$LaPt_4Ge_{11.5}Sb_{0.5}$	$LaPt_4Ge_{11.5}Sb_{0.5}$	8.6729	6.1	23.7	66.9	3.4
800°C 10d						
$LaPt_4Ge_{12}$	$LaPt_4Ge_{12}$	8.6254	6.4	23.4	70.2	0.0
$LaPt_4Ge_{11}Sb$	$LaPt_4Ge_{11}Sb$	8.6888	-	-	-	-
$LaPt_4Ge_{10}Sb_2$	$LaPt_4Ge_{10}Sb_2$	8.7586	-	-	-	-
$LaPt_4Ge_9Sb_3$	$LaPt_4Ge_9Sb_3$	8.7998	6.2	23.4	52.6	17.9
$LaPt_4Ge_8Sb_4$	$LaPt_4Ge_8Sb_4$	8.8529	-	-	-	-
$LaPt_4Ge_7Sb_5$	$LaPt_4Ge_7Sb_5$	8.9075	5.7	23.3	41.8	29.1
$LaPt_4Ge_6Sb_6$	$LaPt_4Ge_7Sb_5$	8.9092	6.4	23.6	41.0	29.0
$LaPt_4Ge_5Sb_7$	$LaPt_4Ge_7Sb_5$	8.9092	5.7	23.4	42.3	28.6
$LaPt_4Ge_7Sb_5$	$LaPt_4Ge_7Sb_5$	8.9084	5.8	23.3	41.1	29.9
$LaPt_4Ge_7Sb_5$	$LaPt_4Ge_7Sb_5$	8.9089	5.6	23.5	40.9	29.9
$LaPt_4Ge_{11.75}Sb_{0.25}$	$LaPt_4Ge_{11.75}Sb_{0.25}$	8.6412	6.1	23.4	69.1	1.5
$LaPt_4Ge_{11.5}Sb_{0.5}$	$LaPt_4Ge_{11.5}Sb_{0.5}$	8.6589	6.0	23.7	67.2	3.0

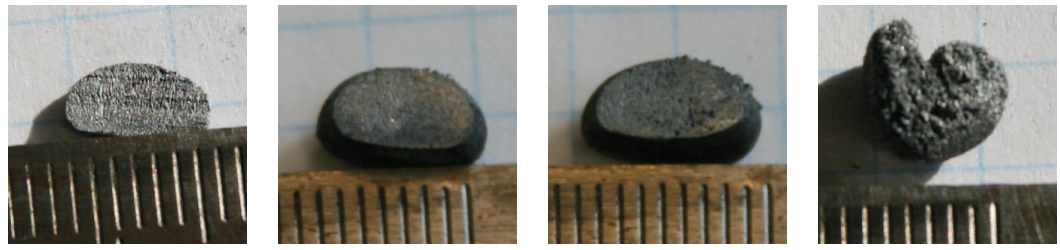

(a) $LaPt_4Ge_{12}$ (b) $LaPt_4Ge_{11.75}Sb_{0.25}$ (c) $LaPt_4Ge_{11.5}Sb_{0.5}$ (d) $LaPt_4Ge_{11}Sb_1$

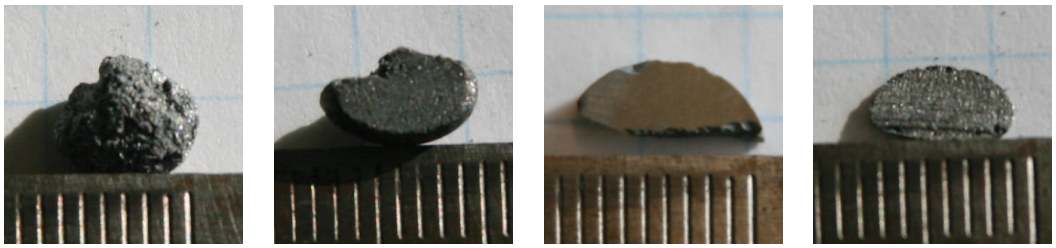

(e) $LaPt_4Ge_{10}Sb_2$ (f) $LaPt_4Ge_9Sb_3$ (g) $LaPt_4Ge_8Sb_4$ (hot pressed) (h) $LaPt_4Ge_7Sb_5$

Figure A.1.: images of the sample series $LaPt_4Ge_{12-x}Sb_x$ after annealing for 10 days at 800°C. Some of the samples are very brittle, even to brittle to cut and measure properties like resistivity, ...

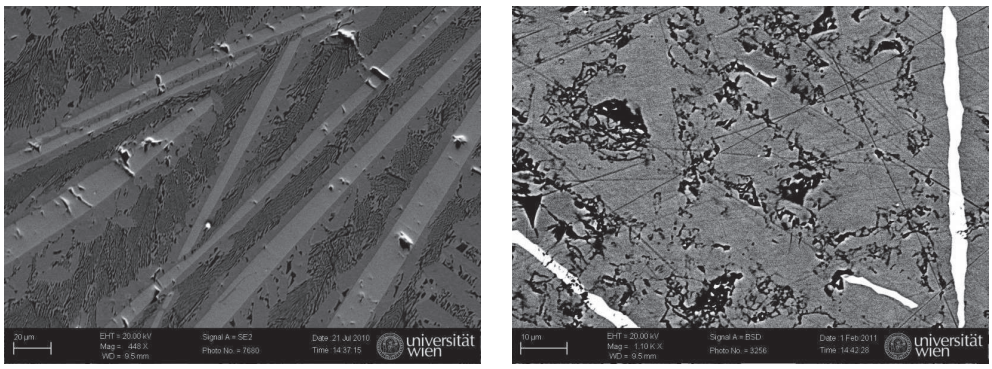

(a) as cast condition (b) annealed 800°C

Figure A.2.: SE/BSE images of the reference sample with the nominal composition $LaPt_4Ge_{12}$ with different heat treatment

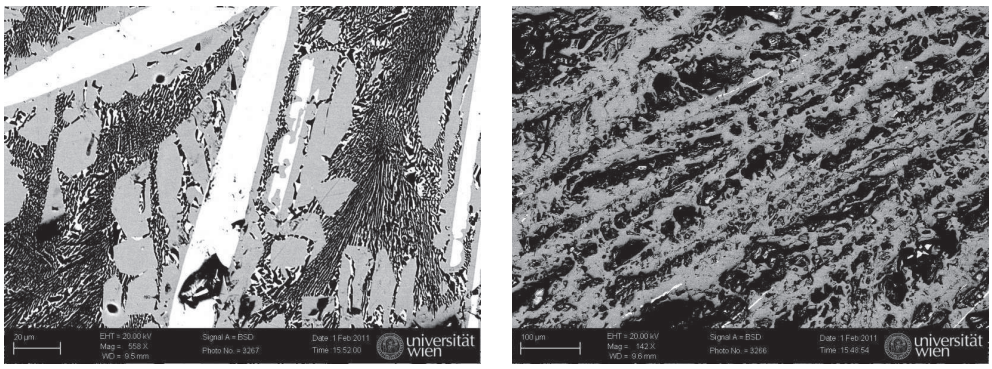

(a) as cast condition (b) annealed 800°C

Figure A.3.: BSE images of the sample with the nominal composition $LaPt_4Ge_{11.75}Sb_{0.25}$ with different heat treatment

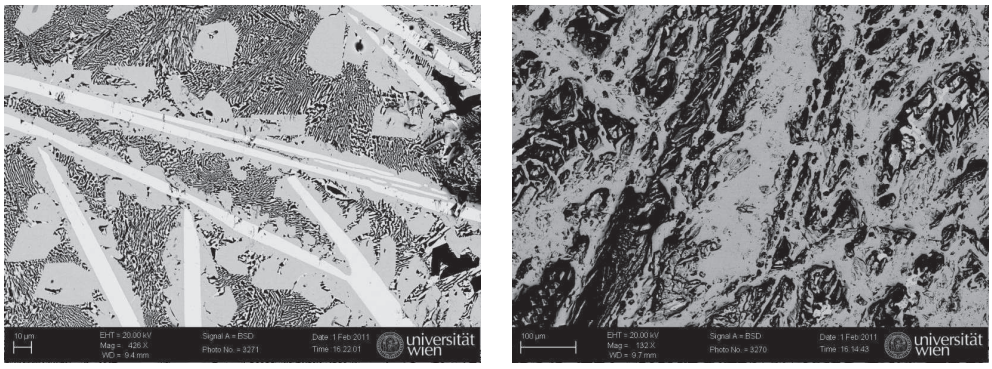

(a) as cast condition (b) annealed 800°C

Figure A.4.: BSE images of the sample with the nominal composition $LaPt_4Ge_{11.5}Sb_{0.5}$ with different heat treatment

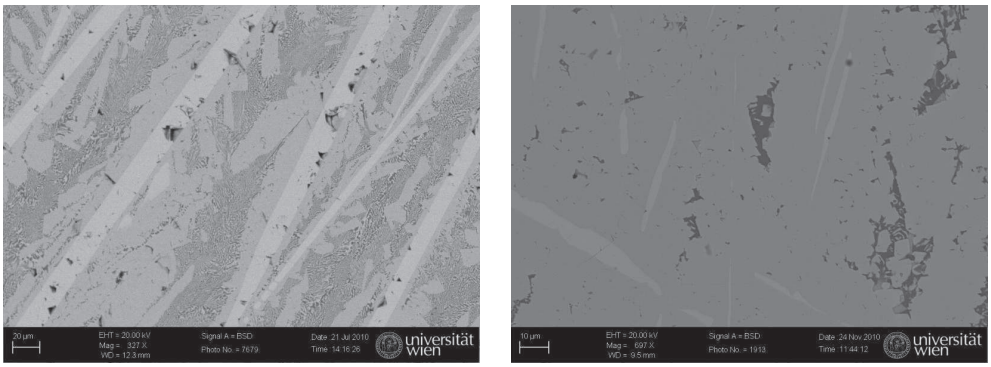

(a) $LaPt_4Ge_{11}Sb_1$ (b) $LaPt_4Ge_{10}Sb_2$

Figure A.5.: BSE images of the samples with the nominal composition $LaPt_4Ge_{11}Sb_1$ and $LaPt_4Ge_{10}Sb_2$ in as cast condition. They could not be analyzed after annealing, because they became to brittle

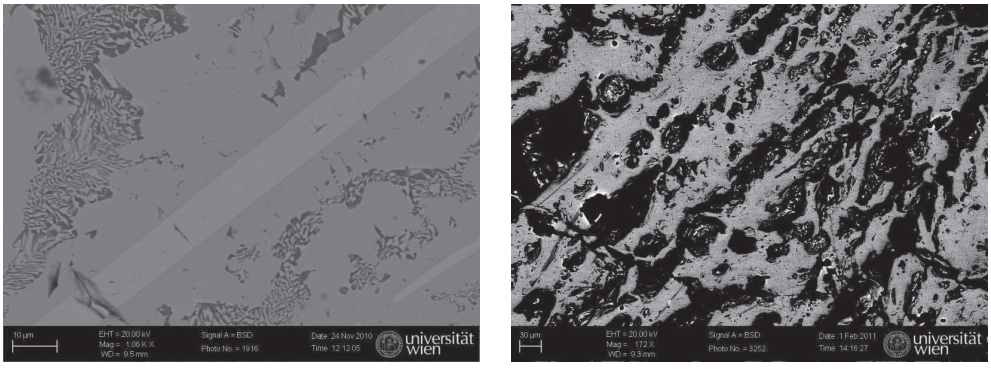

(a) as cast condition (b) annealed 800°C

Figure A.6.: BSE images of the sample with the nominal composition $LaPt_4Ge_9Sb_3$ with different heat treatment

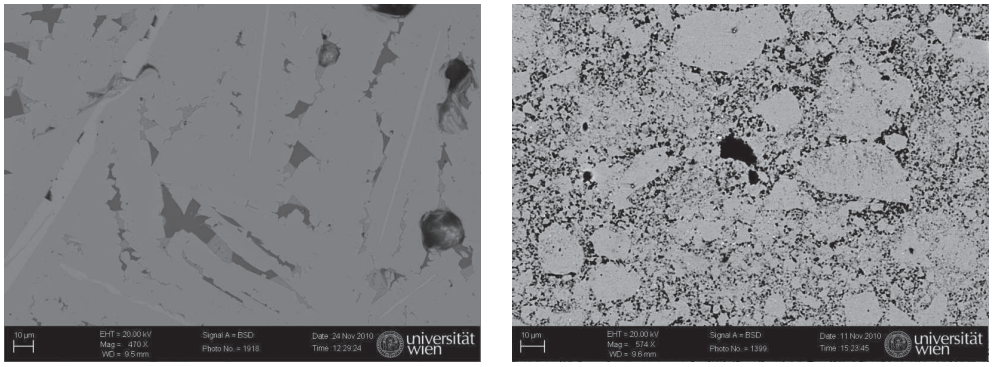

(a) as cast condition (b) hot pressed

Figure A.7.: BSE images of the sample with the nominal composition $LaPt_4Ge_8Sb_4$ with in as cast condition and after hot pressing

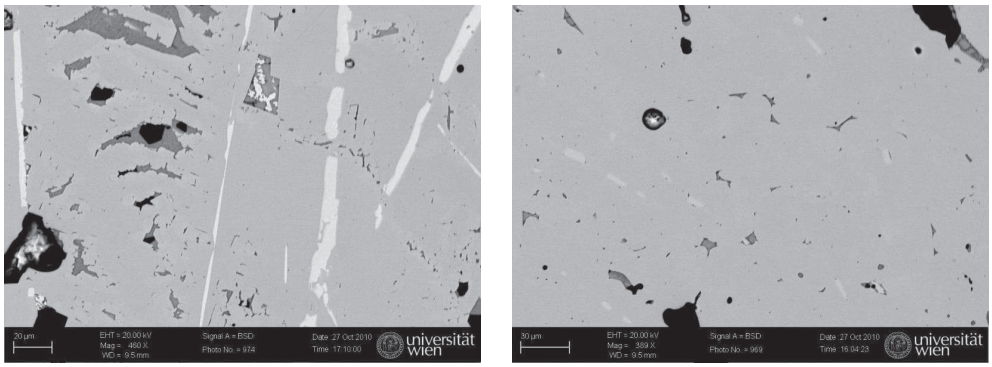

(a) as cast condition (b) annealed 800°C

Figure A.8.: BSE images of the sample with the nominal composition $LaPt_4Ge_7Sb_5$ with different heat treatment

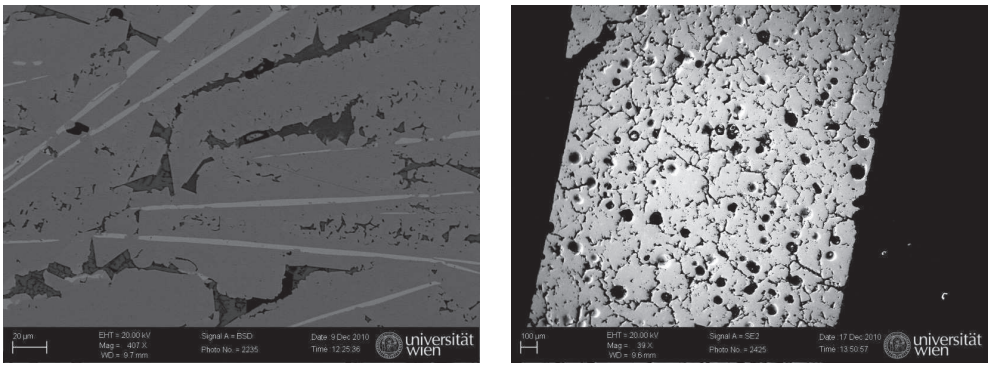

(a) as cast condition

(b) annealed 800°C

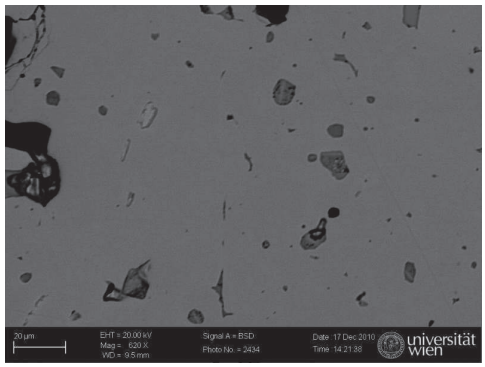

(c) annealed 800°C

Figure A.9.: SE/BSE images of the sample with the nominal composition $LaPt_4Ge_{6.9}Sb_{5.1}$ with different heat treatment

B. Appendix - pictures -tables BaPtIrGe

(a) as cast condition

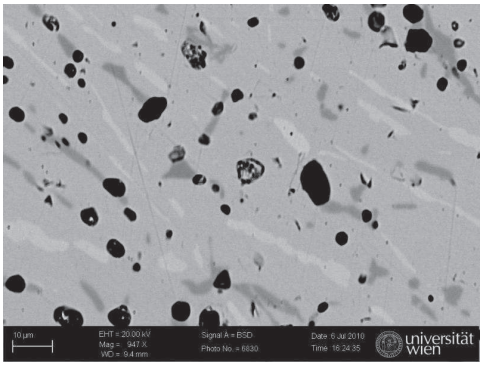

(b) annealed 800°C 10d

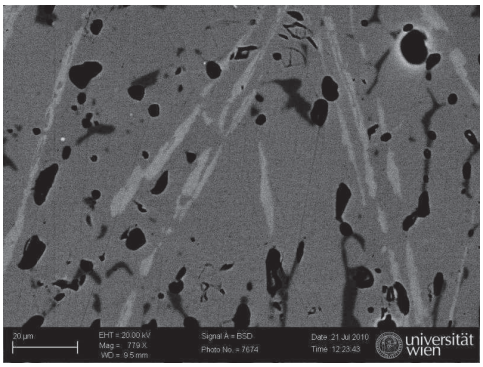

(c) annealed 700°C 10d

Figure B.1.: BSE images of the sample with the nominal composition $BaPt_{3,5}Ir_{0,5}Ge_{12}$ with different heat treatment

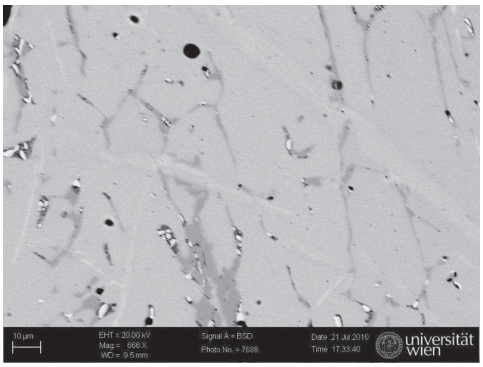

(a) as cast condition

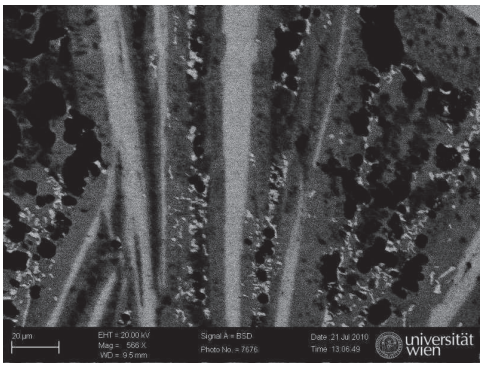

(b) Wärmebehandlung 700°C

Figure B.2.: BSE images of the sample with the nominal composition $BaPt_3Ir_1Ge_{12}$ with different heat treatment

Table B.1.: EDX and X-ray phase analysis data of the sample $BaPt_{3,5}Ir_{0,5}Ge_{12}$; The nominal at% composition of $BaPt_{3,5}Ir_{0,5}Ge_{12}$ is: Ba 5.9, Pt 20.6, Ir 2.9, Ge 70.6

phase	lattice parameter			EDX (at%)			
	a	b	c	Ba	Pt	Ir	Ge
as cast							
$BaPt_4Ge_{12}$	8.6935	8.6935	8.6935	5.7	19.9	0.9	74.2
$Ge/PtGe_2$	5.7877[1,2]	6.1931	2.9089	0.1	16.2	0.8	82.9
$BaIr_xPt_{2-x}Ge_7$	-	-	-	12.3	15.4	5.4	67.0
$IrGe_4$	6.2158[1]	6.2158	7.7939	0.0	5.5	13.9	80.6
700°C 10d							
$BaPt_4Ge_{12}$	8.691	8.691	8.691	6.2	21.2	0.1	72.6
$BaIr_xPt_{2-x}Ge_7$	-	-	-	11.2	16.3	4.5	68.0
$IrGe_4$	6.2127[1]	6.2127	7.7876	0.9	2.5	16.9	80.2
800°C 10d							
$BaPt_4Ge_{12}$	8.6915	8.6915	8.6915	6.1	20.4	0.1	73.4
$BaIr_xPt_{2-x}Ge_7$	-	-	-	10,4	14,9	5.8	69.0
$IrGe_4$	-	-	-	0.1	1.4	17.2	81.4

[1] gained from rietveld refinement
[2] $PtGe_2$

Table B.2.: EDX and X-ray phase analysis data of the sample $BaPt_3Ir_1Ge_{12}$; The nominal at% composition of $BaPt_3Ir_1Ge_{12}$ is: Ba 5.9, Pt 17.6, Ir 5.9, Ge 70.6

phase	lattice parameter			EDX (at%)			
	a	b	c	Ba	Pt	Ir	Ge
as cast							
$BaPt_4Ge_{12}$	8.6943	8.6943	8.6943	6.1	20.9	0.0	73.1
$PtGe_2$	-	-	-	-	29.0	-	71.0
$BaIr_xPt_{2-x}Ge_7$	-	-	-	10.6	15.1	6.1	68.2
700°C 10d							
$BaPt_4Ge_{12}$	8.6837	8.6837	8.6837	6.0	20.8	-	73.2
$IrGe_4$	6.4752[1]	6.4752	8.1166	-	-	-	-
$BaIr_xPt_{2-x}Ge_7$	-	-	-	11.8	14.0	6.7	67.5
800°C 10d							
$BaPt_4Ge_{12}$	8.6985	8.6985	8.6985	6.0	20.1	0.3	73.7
$BaIr_xPt_{2-x}Ge_7$	-	-	-	10.6	15.1	6.1	68.2
$IrGe_4$	6.4697[1]	6.4697	8.1085	0.1	1.3	17.3	81.4
Ir_3Ge_7	-	-	-	0.1	0.2	27.6	72.1
$Pt_{0.5}Ir_{0.5}Ge$	-	-	-	0.1	22.6	25.6	51.7

[1] gained from rietveld refinement

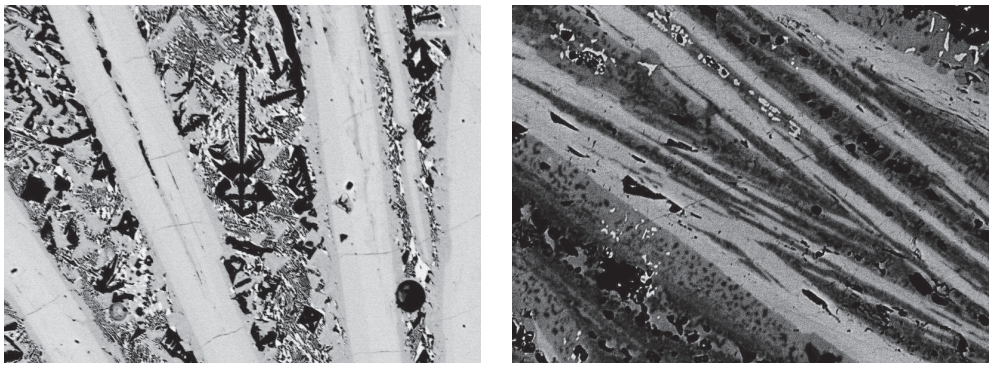

(a) as cast condition (b) annealed 700°C

Figure B.3.: BSE images of the sample with the nominal composition $BaPt_{2,5}Ir_{1,5}Ge_{12}$ with different heat treatment

Table B.3.: EDX and X-ray phase analysis data of the sample $BaPt_{2,5}Ir_{1,5}Ge_{12}$; The nominal at% composition of $BaPt_{2,5}Ir_{1,5}Ge_{12}$ is: Ba 5.9, Pt 14.7, Ir 8.8, Ge 70.6

phase	lattice parameter			EDX (at%)			
	a	b	c	Ba	Pt	Ir	Ge
as cast							
$BaPt_4Ge_{12}$	8.6962	8.6962	8.6962	5.3	18.9	1.5	74.4
$Ge/PtGe_2$	-	-	-	0.2	15.1	1.8	83.0
$BaIr_xPt_{2-x}Ge_7$	-	-	-	12.0	14.8	6.1	67.1
Ge	-	-	-	0.1	0.0	0.1	99.8
Ge_7Pt_3	-	-	-	0.2	27.7	2.7	69.4
$IrGe_4$	6.4825[1]	6.4825	8.1013	-	-	-	-
700°C 10d							
$BaPt_4Ge_{12}$	8.691	8.691	8.691	6.1	20.9	-	73.0
$BaIr_xPt_{2-x}Ge_7$	-	-	-	12.3	12.8	8.1	66.7
Ge	-	-	-	0.1	0.0	0.1	99.8
Ge_7Ir_3	-	-	-	-	-	27.0	73.1
$IrGe_4$	6.4732[1]	6.4732	8.1136	0.4	2.2	17.1	80.4
800°C 10d							
$BaPt_4Ge_{12}$	8.6963	8.6963	8.6963	5.5	17.3	-	77.3
$BaIr_xPt_{2-x}Ge_7$	-	-	-	10.2	13.4	7.0	69.4
$IrGe_4$	6.4776[1]	6.4776	8.1219	-	-	-	-

[1] gained from rietveld refinement

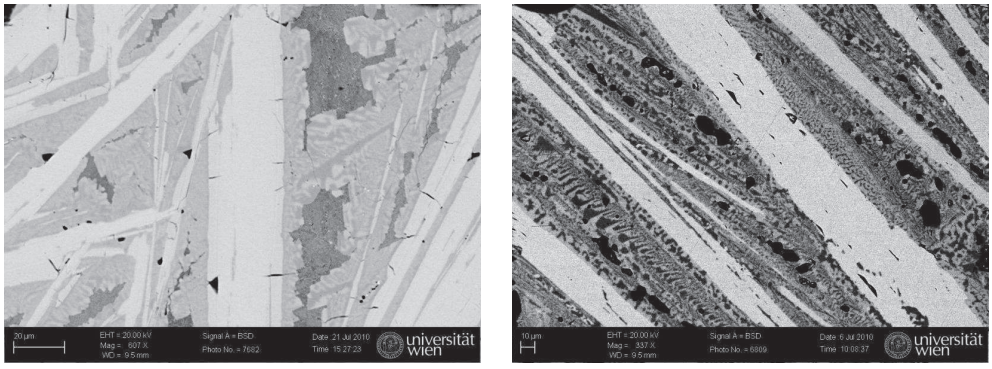

(a) as cast condition (b) annealed 800°C

Figure B.4.: BSE images of the sample with the nominal composition $BaPt_2Ir_2Ge_{12}$ with different heat treatment

Table B.4.: EDX and X-ray phase analysis data of the sample $BaPt_2Ir_2Ge_{12}$; The nominal at% composition of $BaPt_2Ir_2Ge_{12}$ is: Ba 5.9, Pt 11.8, Ir 11.8, Ge 70.6

phase	lattice parameter			EDX (at%)			
	a	b	c	Ba	Pt	Ir	Ge
as cast							
$BaPt_4Ge_{12}$	8.7016	8.7016	8.7016	10.5	9.9	11.0	68.6
$Ge/PtGe_2$	-	-	-	-	17.1	-	83.0
$BaIr_xPt_{2-x}Ge_7$	-	-	-	10.5	9.9	11.0	68.6
800°C 10d							
$BaPt_4Ge_{12}$	8.6926	8.6926	8.6926	6.0	20.2	0.6	73.6
$BaIr_xPt_{2-x}Ge_7$	-	-	-	10.1	11.1	10.1	68.7
$IrGe_4$	6.476[1]	6.476	8.116	0.2	1.0	17.7	81.3

[1] gained from rietveld refinement

C. User defined functions for tablecurve

C.1. Heat capacity

C.1.1. Debye model

#F1 = $^4*EXP($)/(EXP($)-1)^2
#F2 = #B/X
Y=#A*X+(9*8.314*17/#F2^3)*QIN(1,0.001,#F2,12)
Y ... C_P
#A ... gamma value of the specific heat
#B ... Debye Temperature

C.1.2. Debye Einstein model

R=8.314
#F1 = #A/X
#F2 = 3*R*17* EXP(#F1)*#F1^2 /(EXP(#F1)-1)^2
#F3 =$^4*EXP($)/(EXP($)-1)^2
#F4 =#B/X
#F5 =(9*17*R/#F4^3)*QIN(3,0.001,#F4,12)
Y=#C*X+#F2*((#D-3)/#D) + #F5*(3/#D)
Y ... $\mathrm{C_P}$
#A ... Einstein temperature
#B ... Debye temperature
#C ... gamma value of the specific heat
#D ... number of modes

C.1.3. Debye Einstein2 model

R = 8.314
#F1 = #A/X
#F2 = 3*R*17* EXP(#F1)*#F1^2 /(EXP(#F1)-1)^2
#F3 = #E/X
#F4 = 3*R*17* EXP(#F3)*#F3^2 /(EXP(#F3)-1)^2
#F5 = $^4*EXP($)/(EXP($)-1)^2
#F6 = #B/X
#F7 = (9*17*R/#F6^3)*QIN(5,0.001,#F6,12)
Y = #C*X + #F2*((#D)/(#F+#D+3)) + #F4*((#F)/(#F+#D+3)) + #F7*(3/(#F+#D+3))
Y ... C_P
#A ... Einstein temperature 1
#B ... Debye temperature
#C ... gamma value of the specific heat
#D ... number of modes at Einstein temperature 1
#E ... Einstein temperature 2
#F ... number of modes at Einstein temperature 2

C.1.4. Debye Einstein3 model

R = 8.314
#F1 = #A/X
#F2 = 3*R*17* EXP(#F1)*#F1^2 /(EXP(#F1)-1)^2
#F3 = #E/X
#F4 = 3*R*17* EXP(#F3)*#F3^2 /(EXP(#F3)-1)^2
#F5 = $^4*EXP($)/(EXP($)-1)^2
#F6 = #G/X
#F7 = 3*R*17* EXP(#F6)*#F6^2 /(EXP(#F6)-1)^2
#F8 = #B/X
#F9 = (9*17*R/#F8^3)*QIN(5,0.001,#F8,12)
Y = #C*X + #F2*((#D)/(#F+#D+#H+3)) + #F4*((#F)/(#F+#D+#H+3)) + #F7*((#H)/(#F+#D+#H+3)) +#F9*(3/(#F+#D+#H+3))
Y ... C_P

#A ... Einstein temperature 1
#B ... Debye temperature
#C ... gamma value of the specific heat
#D ... number of modes at Einstein temperature 1
#E ... Einstein temperature 2
#F ... number of modes at Einstein temperature 2
#G ... Einstein temperature 3
#H ... number of modes at Einstein temperature 3

C.2. Thermal expansion after Mukherjee

C.2.1. Debye model for the internal energy

#F1=$^3/(EXP($)-1)
#F2=#A1/X
#F3=9*8.314*X/#F2^3*QIN(1,0.01,#F2,12)
#F5=#F3
Y=#A0*X^2+#A2*(#F5-#A3*#F5^2-#A4*#F5^3)
Y ... dl/l_0 #A0 ... $\frac{\gamma}{2}$ electronic contribution
#A1 ... Debye temperature
#A2 ... $\frac{3g}{4c^2}$ constants. g proportional to the cubic anharmonicity, c prop to the harmonic
#A3 ... G some constant including the strength of the anharmonicity of the cubic and the quarternic and the harmonic part
#A4 ... F some constant including the strength of the anharmonicity of the cubic and the quarternic and the harmonic part

C.2.2. Debye Einstein model for the internal energy

#F1=$^3/(EXP($)-1)
#F2=#A1/X
#F3=9*8.314*X/#F2^3*QIN(1,0.01,#F2,12)
#F4=3*8.314*#A6/(EXP(#A6/X)-1)
#F5=3/(#A5+3)*#F3+#A5/(#A5+3)*#F4

Y=#A0*X^2+#A2*(#F5-#A3*#F5^2-#A4*#F5^3)
Y ... $\mathrm{dl/l_0}$
#A0 ... $\frac{\gamma}{2}$ electronic contribution
#A1 ... Debye temperature
#A2 ... p average number of phonon branches that are excited over this temperature range
#A3 ... Einstein temperature
#A4 ... $\frac{3g}{4c^2}$ constants. g proportional to the cubic anharmonicity, c prop to the harmonic
#A5 ... G some constant including the strength of the anharmonicity of the cubic and the quarternic and the harmonic part
#A6 ... F some constant including the strength of the anharmonicity of the cubic and the quarternic and the harmonic part

C.3. Resistivity

C.3.1. Bloch- Grüneisen model

#F1=$^5/(EXP(-$)+EXP($)-2)
#F2=#A2/X Y=#A0+4*#A1*QIN(1,0.01,#F2,12)/#F2^5 Y ... $\rho(\mathrm{T})$
#A0 ... ρ_0 residual resistivity
#A1 ... electron phonon interaction constant R
#A2 ... Debye temperature Θ_D

C.3.2. 2-Band model

#F1=$^5/(EXP(-$)+EXP($)-2)
#F2=#A2/X
#F3=#A0+4*#A1*QIN(1,0.01,#F2,12)/#F2^5
#F4=-#A4+X*(LN(2)+LN(EXP((#A3+#A4)/X)+1)-LN(EXP(#A3/X)+1))
#F5=LN(2)*X
#F6=#A5*SQRT(#F4*F5)+#A6
Y=#A6/#F6*#F3
Y ... $\rho(\mathrm{T})$

#A0 ... ρ_0 residual resistivity
#A1 ... electron phonon interaction constant R
#A2 ... Debye temperature Θ_D
#A3 ... E_1 energy difference between Fermi level and energy gap
#A4 ... E_g energy gap
#A5 ... $\mathrm{k_B N}$ number of states in units of $\mathrm{k_B}$
#A6 ... n_0

C.4. Thermal conductivity

F = 2.8526*10^8;
F1=#A0*$^4*X^4;
F2=#A1*$^2*X^3*EXP(-#A4/(3*X));
F3=#A2;
F4=#A3*X*$;
F5=1/(F1+F2+F3+F4)
F9= ($^4*EXP($)/(EXP($) - 1)^2)*F5
Y=(F*X^3/#A4)*AI(9, 0, (#A4/X))+#A5*X^3
Y ... $\lambda_\mathrm{p}\mathrm{h}$ + radiation loss
#A0 ... defect scattering process parameter $[\frac{1}{\mathrm{K^4 s}}]$
#A1 ... Umklapp process parameter $[\frac{1}{\mathrm{K^3 s}}]$
#A2 ... boundaries scattering parameter $[\frac{1}{\mathrm{s}}]$
#A3 ... phonon- electron scattering parameter $[\frac{1}{\mathrm{Ks}}]$
#A4 ... Debye Temperature Θ_D $[\mathrm{K}]$
#A5 ... parameter for correction of radiation losses

References

[1] MacDonald D.K.C. *Thermoelectricity: an introduction to the principles*. John Wiley & Sons, Inc., 1961.

[2] C. B. Vining. An inconvenient truth about thermoelectrics. *Nature Materials*, 8:83 – 85, 2009.

[3] Rowe D.M. *CRC Handbook of THERMOELECTRICS*. CRC Press LLC, 1995.

[4] RIT. *http://edge.rit.edu/content/P09451/public/Home*. 2011.

[5] L.P. Lévy. *Magnetism and Superconductivity*. Springer-Verlag Berlin Heidelburg New York, 1997.

[6] E. Royanian. *Phase instabilities in strongly correlated Ce-Pt-Si materials and superconductivity in novel Ge-based skutterudites* $(\mathrm{Ba}, \mathrm{Sr}, \mathrm{Th})\mathrm{Pt}_4\mathrm{Ge}_{12}$. PhD thesis, TU Vienna, 2008.

[7] Fossheim K. and Sudbø A. *Superconductivity: Physics And Applications*. John Wiley & Sons, London, 2004.

[8] H.W. Weber and O. Hittmair. *Supraleitung*. Karl Thiemig München, 1979.

[9] G.Hilscher. Festkörperphysik 1; Magnetismus & Supraleitung. lecture notes, Institute of solid state physics, TU Vienna, 2009.

[10] University of Birmingham. *http://www.cm.ph.bham.ac.uk/scondintro/basicscintro.html*. 2011.

[11] A. A. Abrikosov. Nobel Lecture: Type-II superconductors and the vortex lattice. *Reviews of Modern Physics*.

[12] A. F. May E. S. Toberer and G. J. Snyder. Zintl chemistry for designing high efficiency thermoelectric materials. *Chem. Mater.*, 22(3):624634, Jul 2010.

[13] Julian H. Goldsmid. *Introduction to Thermoelectricity*. Springer Series in Material Science, Springer Heidelberg, Dordrecht, London, New York, 2010.

[14] G. J. Snyder and E. S. Toberer. Complex thermoelectric materials. *Nature Materials*, 7:105 – 114, 2008.

[15] Xing-Qiu Chen N. Melnychenko-Koblyuk G. Hilscher H. Kaldarar H. Michor E. Royanian G. Giester M. Rotter R. Podloucky E. Bauer, A. Grytsiv and P. Rogl. Superconductivity in novel Ge-based skutterudites: $(\mathrm{Sr,Ba})\mathrm{Pt_4Ge_{12}}$. *Physical Review Letters*, 99(21):217001–1 – 217001–4, Nov 2007.

[16] S. R. Brown S. M. Kauzlarich and G. J. Snyder. Zintl phases for thermoelectric devices. *Dalton Transactions*, pages 2099–2107, April 2007.

[17] H. Rosner M. Nicklas A. Leithe-Jasper R. Gumeniuk, W. Schnelle and Yu. Grin. Superconductivity in the platinum germanides $\mathrm{MPt_4Ge_{12}}$ (M=rare-earth or alkaline-earth metal) with filled skutterudite structure. *Phys. Rev. Lett.*, 100(1):017002, Jan 2008.

[18] Fließbach T. *Statistische Physik*. Spektrum Akademischer Verlag, 4 edition.

[19] E. Bauer. Transportphänomene in Festkörperphysik. lecture notes, Institute of solid state physics, TU Vienna, 2006.

[20] David M. [Ed.] Rowe. *CRC Handbook of Thermoelectrics*. CRC Press LLC, Boca Raton, 1995.

[21] Zavarsky A. Van der pauw resistivity measurement and thermoelectric properties of $\mathrm{Ba_8Zn_xNi_yGe_{46-x-y}}$. Master's thesis, TU Vienna, Karlsplatz 8, 1040 Wien, 2010.

[22] E. Bauer. Thermoelectric materials and applications. lecture notes, Institute of solid state physics, TU Vienna, 2008.

[23] Bednar I. Thermoelectric properties of novel clathrates. Master's thesis, TU Vienna, Karlsplatz 8, 1040 Wien, 2010.

[24] Charles Kittel. *Einführung in die Festkörperphysik*. Oldenbourg Verlag München Wien, 14. edition, 2006.

[25] M.Reissner G.Hilscher, H.Michor. Festkörperphysik 1; Teil1: Phononen, Elekronen. lecture notes, Institute of solid state physics, TU Vienna, 2009.

[26] Louie S.G. Chelikowsky J.R. *Quantum theory of real materials*. Number 17. Kluwer, Boston.

[27] J. Callaway. Model for lattice thermal conductivity at low temperatures. *Phy. Rev.*, 113(4):1046 – 1051, Feb 1959.

[28] Ioffe A.F. *Halbleiter-Thermoelemente*. Akademie-Verlag Berlin, 1957.

[29] Peter Hadley. *http://lamp.tu-graz.ac.at/h̃adley/ss1/phonons/phonontable.html*. TU Graz, 2011.

[30] Gerda Rogl. *Development of Skutterudites with High Thermoelectric and Mechanical Properties by Filling and Nanocrystallization*. PhD thesis, University of Vienna, 2011.

[31] C. Bansal Goutam Dev Mukherjee and Ashok Chatterjee. Thermal expansion study of ordered and disordered $\mathrm{Fe_3Al}$: An effective approach for the determination of vibrational entropy. *Phys. Rev. Lett.*, 76(11):1876–1879, Mar 1996.

[32] Mermin David N. Ashcroft Neil W. *Festkörperphysik*. Oldenbourg Verlag München Wien, 3. edition, 2007.

[33] Falmbigl M. Thermoelectricity of inverse clathrates. Master's thesis, Universität Wien, 2008.

[34] Stefan Berger. *Novel thermoelectric materials*. PhD thesis, TU Vienna, 2003.

[35] Schaudy G. *Kalorimetrie in hohen Magnetfeldern*. PhD thesis, TU Vienna, 1995.

[36] E. Gratz M. Doerr M. Rotter, H. Müller and M. Loewenhaupt. A miniature capacitance dilatometer for thermal expansion and magnetostriction. *Review of scientific instruments*, 69(7):2742 – 2746, Jul 1998.

[37] G.D. Cody D.W. Woodard. Anomalous resistivity of $\mathrm{Nb_3Sn}$. *Phys. Rev.*, 136(1A):A166–A168, Oct 1964.